Title

Dendritic spine morphology regulates calcium-dependent synaptic weight change

Journal

The Journal of General Physiology, 154(8)

ISSN

0022-1295

Authors

Bell, Miriam K
Holst, Maven V
Lee, Christopher T
et al.

Publication Date

2022-08-01

DOI

10.1085/jgp.202112980

Peer reviewed

JGP Journal of General Physiology

ARTICLE

Dendritic spine morphology regulates calcium-dependent synaptic weight change

Miriam K. Bell[1]*, Maven V. Holst[1]*, Christopher T. Lee[1], and Padmini Rangamani[1]

Dendritic spines act as biochemical computational units and must adapt their responses according to their activation history. Calcium influx acts as the first signaling step during postsynaptic activation and is a determinant of synaptic weight change. Dendritic spines also come in a variety of sizes and shapes. To probe the relationship between calcium dynamics and spine morphology, we used a stochastic reaction-diffusion model of calcium dynamics in idealized and realistic geometries. We show that despite the stochastic nature of the various calcium channels, receptors, and pumps, spine size and shape can modulate calcium dynamics and subsequently synaptic weight updates in a deterministic manner. Through a series of exhaustive simulations and analyses, we found that the calcium dynamics and synaptic weight change depend on the volume-to-surface area of the spine. The relationships between calcium dynamics and spine morphology identified in idealized geometries also hold in realistic geometries, suggesting that there are geometrically determined deterministic relationships that may modulate synaptic weight change.

Introduction

Dendritic spines are small protrusions along the dendrites of neurons that compartmentalize postsynaptic biochemical, electrical, and mechanical responses. These subcompartments house the majority of excitatory synapses and are key for neuronal communication and function (Nishiyama and Yasuda, 2015; Murakoshi and Yasuda, 2012). Because of their unique biochemical compartmentation capabilities, spines are thought of as computational units that can modify their synaptic strength through a process called synaptic plasticity (Yuste and Denk, 1995; Nishiyama and Yasuda, 2015). There have been many different approaches, both experimental and computational, to understand how these small subcompartments of excitatory neurons can regulate learning and memory formation (Lee et al., 2012; Segal, 2010). These studies have helped identify a few key scientific threads: (1) the biochemical signal transduction cascades in spines span multiple time scales, but Ca^{2+} is the critical initiator of these events; (2) spines have distinct morphological features that can be categorized depending on physiological or pathological conditions (Table 1; Kasai et al., 2003); and (3) synaptic weight update is a measure of the strength of a synapse and represents the strength of the connection between neurons. Synaptic weight represents changes to synaptic connection strength that occurs during synaptic plasticity, such as during long-term potentiation (LTP) and long-term depression (LTD; Lee et al., 2012). In this work, we focus on bridging these different ideas by asking the following question: how does spine morphology affect synaptic weight update? To answer this question, we develop a computational model that focuses on the stochastic dynamics of Ca^{2+} in spines of different geometries and map the synaptic weight update to geometric parameters.

Calcium plays a key role as a second messenger in biochemical and physical modifications during synaptic plasticity, triggering downstream signaling cascades within dendritic spines and the entire neuron (Yuste and Denk, 1995; Yuste et al., 2000; Augustine et al., 2003). Theoretical efforts have linked calcium levels to synaptic plasticity change through a parameter called synaptic weight that essentially captures the strength of the synapse (Jahr and Stevens, 1993; Shouval et al., 2002; Graupner and Brunel, 2012; O'Donnell et al., 2011). An increase in synaptic weight is associated with synapse strengthening, while a decrease in synaptic weight is associated with synapse weakening (Lisman, 2017; Earnshaw and Bressloff, 2006). While changes in synaptic strength require a host of downstream signaling and mechanical interactions (Xia and Storm, 2005; Mäki-Marttunen et al., 2020), the level of calcium is a well-accepted indicator of synaptic plasticity and weight (Shouval et al., 2002; Jędrzejewska-Szmek et al., 2017). This led to the hypothesis that synaptic plasticity outcome could be determined from the calcium dynamics alone; this theory has been readily used for numerous models in computational neuroscience

[1]Department of Mechanical and Aerospace Engineering, University of California San Diego, La Jolla, CA.

*M.K. Bell and M.V. Holst contributed equally to this paper. Correspondence to Padmini Rangamani: prangamani@ucsd.edu.

Table 1. **Geometric parameters of different spine morphologies**

Parameter	Filopodia[a]	Thin[b]	Mushroom[c]
Total length (L; μm)	2–20	0.98 ± 0.42	1.5 ± 0.25
Length of neck (l; μm)		0.51 ± 0.34	0.43 ± 0.21
Neck diameter ($2r$; μm)	< 0.3	0.1 ± 0.03	0.2 ± 0.07
Total volume (μm^3)		0.04 ± 0.02	0.29 ± 0.13
Volume of head (V; μm^3)		0.03 ± 0.015[d]	0.27 ± 0.13
Total surface area (μm^2)		0.59 ± 0.29	2.7 ± 0.93
Surface area of PSD (μm^2)		0.05 ± 0.02	0.3 ± 0.1

Table modified from Alimohamadi et al. (2021).
[a]Yuste and Bonhoeffer (2004); Kanjhan et al. (2016).
[b]Harris et al. (1992); Rodriguez et al. (2008); Spacek and Harris (1997).
[c]Harris et al. (1992); Spacek and Harris (1997).
[d]Value from Harris et al. (1992) was 0.03 ± 0.15, but we assume there was a typo in the original text because the spine volume should not be negative.

(Shouval et al., 2002; Mahajan and Nadkarni, 2019). Because of their probabilistic nature and discrete number, calcium ion channels and receptors appear to behave stochastically (Anwar et al., 2013; Dudman and Nolan, 2009; Faisal et al., 2005). This indicates that calcium dynamics in the spine leans toward stochasticity, and it has been suggested that synaptic plasticity itself relies on stochasticity for robustness (Cannon et al, 2010; O'Donnell et al, 2011; Anwar et al, 2013; Koumura et al, 2014; O'Donnell and Nolan, 2014; Fujii et al, 2017; Tottori et al, 2019). In this work, we seek to understand how spine morphology can modulate synaptic weight update predicted through stochastic calcium dynamics.

Dendritic spines have characteristic sizes and shapes that dynamically change over time in response to stimulus and are associated with their function and synaptic plasticity (Bourne and Harris, 2008; Holthoff et al., 2002). Just as whole-cell shape is known to influence signaling dynamics (Calizo et al., 2020; Neves et al., 2008; Rangamani et al., 2013; Héja et al., 2021; Bell and Rangamani, 2021; Scott et al., 2021), studies have specifically probed the interplay between calcium dynamics and dendritic spine morphology (Bell et al., 2019; Cugno et al., 2019; Yuste et al., 2000; Bartol et al., 2015). Because of the historical significance of dendritic spines as electrical subcompartments, the morphology of the spine neck has been implicated in regulating calcium signaling, and longer spine necks were found to decouple spine-dendrite calcium signaling (Volfovsky et al., 1999). Additional modeling work coupled actin–myosin contractions to cytoplasmic flow to identify two time scales of calcium motion, driven by flow and diffusion, respectively, that depend on spine geometry (Holcman et al., 2004). A combined analytical and numerical study showed how geometry and curvature gives rise to pseudo-harmonic functions that can predict the locations of maximum and minimum calcium concentration (Cugno et al., 2019). More recently, we used a deterministic reaction-diffusion model to investigate dendritic spine morphology and ultrastructure and found that dendritic spine volume-to-surface-area ratios and the presence of spine apparatus (SpApp) modulate calcium levels (Bell et al., 2019). As we have shown before, the natural length scale that emerges for reaction-diffusion systems with boundary conditions that have influx and efflux rates is the volume-to-surface-area ratio (Calizo et al., 2020; Cugno et al., 2019). What remains unclear is whether the trends from dimensional analysis of deterministic models continue to hold despite the stochastic nature of calcium influx and efflux across the wide range of spine shapes.

In this work, using idealized and realistic spine geometries, we investigate the impact of shape and stochasticity on calcium dynamics and synaptic weight change. We seek to answer the following question: How do specific geometric parameters—namely, shape and size of dendritic spines—influence calcium dynamics and therefore synaptic weight change? To address this question, we built a spatial, stochastic model of calcium dynamics in different dendritic spine geometries. We used idealized geometries informed by the literature to control for the different geometric parameters and then extended our calculations to realistic geometries. We probed the influence of spine shape, volume, and volume-to-surface-area ratio on calcium influx, variance of calcium dynamics, and the robustness of synaptic weight. We show that although calcium dynamics in individual spines are stochastic, synaptic weight changes proportionally with the volume-to-surface-area ratio of the spines, suggesting that there may exist deterministic relationships between spine morphology and strengthening of synapses.

Materials and methods

Model development

Ca^{2+} dynamics in dendritic spines have been previously studied using computational models (Bartol et al., 2015; Friedhoff et al., 2021; Cugno et al., 2019; Bell et al., 2019; Holcman et al., 2005). In this work, we focused on modeling effort on the early, rapid influx on Ca^{2+} for spines of different sizes and shapes with the goal of identifying relationships between spine geometry and early synaptic weight change. Our model is based on previous works (Bartol et al., 2015; Bell et al., 2019; Mahajan and Nadkarni, 2019) with some modifications and simplifications to enable us to identify the relationship between spine morphology and synaptic weight change. Inspired by Bartol et al. (2015), we converted a previous deterministic model of calcium influx (Bell et al., 2019) to a spatial, particle-based stochastic model constructed in Monte Carlo Cell (MCell; Stiles and Bartol, 2001; Stiles et al., 1996; Kerr et al., 2008), to capture the stochastic nature of Ca^{2+} dynamics in the small spine volumes. We specifically focus on dendritic spine geometries and calcium dynamics representative of hippocampal pyramidal neurons (Bell et al., 2019). We detail the steps below.

Assumptions

Here we list the main assumptions in the model and describe the components of the model shown in Fig. 1.

- **Geometries:** We investigate how spine geometry (spine volume, shape, and neck geometry) and ultrastructure (spine apparatus) can influence synaptic weight change, with the goal of drawing relationships between these different morphological features and synaptic weight (Fig. 1 e).

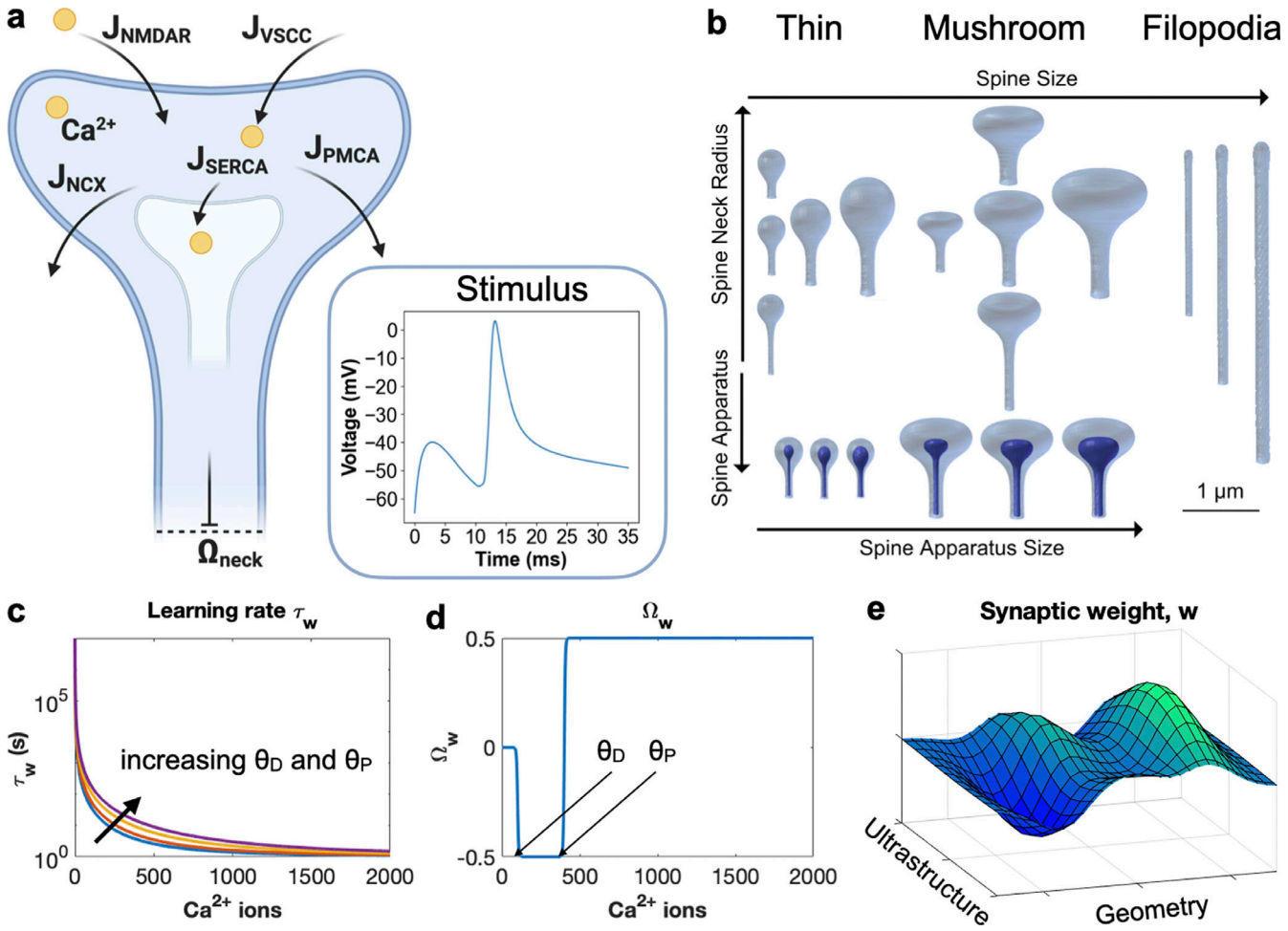

Figure 1. **Model overview. (a)** Our spatial particle–based model includes calcium influx through NMDAR and VSCC and calcium efflux to the extracellular space through PMCA and NCX pumps and to the SpApp through SERCA pumps. Arrows indicate the movement of Ca^{2+} through the labeled pump, channel, or receptor. Ω_{neck} represents the Dirichlet boundary condition at the base of the spine neck, at which the concentration of calcium ions is clamped to zero. Cytosolic calcium was buffered using cytosolic mobile and membrane-bound immobile calcium buffers. Inset: A change in membrane potential triggered by an EPSP and BPAP acts as the model stimulus, along with the release of glutamate molecules. **(b)** The geometric factors considered in our model include spine shape, spine size, neck radius and length, and SpApp size. We investigated three spine shapes: thin, mushroom-, and filopodia-shaped. **(c–e)** Calcium levels determine the learning rate τ_w (c) and function Ω_w (d), that in turn determine synaptic weight (e). The influence of geometry (spine volume, surface area, PSD area, etc.) and ultrastructure (SpApp, internal organelles, etc.) on calcium signaling thus has an influence on synaptic weight. θ_D and θ_P represent the thresholds for LTD and LTP, respectively. Panel a was generated using biorender.com.

• **Idealized geometries:** Idealized geometries of thin, mushroom-shaped, and filopodia-shaped spines were selected from Alimohamadi et al. (2021), and the different geometric parameters are given in Tables S1 and S2 and Fig. 1 b.
– *Postsynaptic density (PSD)*: For each control geometry, the PSD area was set as a fixed proportion of the spine volume.
– *Size variations*: For each spine geometry, we varied the volume of the control geometry to consider the impact of different morphological features.
– *Spine apparatus*: A SpApp is included in the thin and mushroom idealized spines by scaling the spine geometry to a smaller size and including it within the plasma membrane (PM) geometry. These variations were included to modify the volume of the spine in the presence of these organelles.

• **Realistic geometries:** We also investigated how spine morphology affected synaptic weight change in realistic morphologies. Realistic spine morphologies were reconstructed from 3-D EM images (Wu et al., 2017) at sufficient mesh quality to import into MCell (Lee and Laughlin, 2020). Realistic spines were selected to have a variety of morphologies to reflect filopodia-shaped, thin, and mushroom spines. PSDs were denoted based on the segmentation of the original 3-D electron micrographs.

• **Time scales:** Our goal is to consider the initial changes in synaptic weight due to a single calcium pulse, consistent with prior studies (Bartol et al., 2015; Shouval et al., 2002). Our focus is on early time scale events associated with synaptic weight, rather than the induction of LTP/LTD specifically. The time scale of calcium transients is rapid, on the millisecond time scale (Bartol et al., 2015; Holcman et al., 2004; Holcman et al., 2005), owing to the single activation pulse, various buffering components, and the SpApp acting as a calcium sink, rather than a

Table 2. **Parameters used in the model**

Variable	Value	Unit	Reference
Initial $[Ca^{2+}]_{cyto}$	1×10^{-7}	M	Cornelisse et al. (2007); Bartol et al. (2015)
Initial $[Ca^{2+}]_{ER}$	6×10^{-5}	M	Bartol et al. (2015)
Initial $[Ca^{2+}]_{ECS}$	2	mM	Robinson and Stokes (1959)
k_d	50	s^{-1}	Bell et al. (2019)
D_{Ca2+}	2.2×10^{-6}	$cm^2\ s^{-1}$	Griffith et al. (2016); Naraghi and Neher (1997)
$k_{B,on}$	1×10^6	$M^{-1}\ s^{-1}$	Bartol et al. (2015)
$k_{B,off}$	2	s^{-1}	Bartol et al. (2015)
$k_{Bm,on}$	1×10^6	$M^{-1}\ s^{-1}$	Schwaller (2010)
$k_{B,off}$	1	s^{-1}	Schwaller (2010)
$D_{Bm}\ D_{Ca} \cdot B_m$	2×10^{-7}	$cm^2\ s^{-1}$	Griffith et al. (2016)
Initial $[B_m]$	2×10^{-5}	M	Schwaller (2010)
Initial $[B_f]$	4,791	molecule μm^{-2}	Bartol et al. (2015)

The parameters that are passed directly into the MCell model are given in the units native to MCell (M for concentration, $cm^2\ s^{-1}$ for diffusion constants, and molecules μm^{-2} for surface molecule density). These units are converted into particle numbers for each compartment.

source (Basnayake et al., 2019; Basnayake et al., 2021). Each spine geometry is initiated with a basal concentration of calcium as shown in Table 2. For each geometry, these concentrations were converted to numbers of Ca^{2+} ions to initialize the particle-based simulations.

• **Calcium model stimulus:** The stimulus used in the model is an excitatory postsynaptic potential (EPSP) and back-propagating action potential (BPAP) offset by 10 ms and a glutamate release that activates *N*-methyl-D-aspartate receptor (NMDAR; Bartol et al., 2015) as shown in Fig. 1 a, inset. We include the presynapse as a surface from which glutamate is released from a central location. α-Amino-3-hydroxy-5-methyl-4-isoxazolepropionic acid receptor (AMPARs), which competes with NMDARs, to bind glutamate, are also included in the model but do not contribute to the calcium influx.

• **Channel and receptor dynamics:** We assume that the surface density of the receptors and channels on the membrane of the spine is constant and uniformly distributed (Sabatini and Svoboda, 2000; Holthoff et al., 2002). This assumption is based on experimental observations (Sabatini and Svoboda, 2000) and has been used in other computational models of calcium dynamics (Bell et al., 2019; Keller et al., 2008; Franks et al., 2002). An important consequence of this assumption is that when the surface area of the spine changes, the total number of receptors will also change. How calcium influx scales with spine volume is an important consideration with implications on how calcium concentration scales with spine size (O'Donnell et al., 2011). The constant receptor density assumption means that calcium influx undercompensates for increases in spine volume (O'Donnell et al., 2011).

• **Boundary conditions:** Calcium ion influx occurs through NMDAR localized to the PSD region and voltage-sensitive calcium channels (VSCCs) on the PM, based on Bartol et al. (2015). Calcium ions leave the spine volume through the pumps on the PM, plasma membrane Ca^{2+}-ATPase (PMCA), and sodium–calcium exchanger (NCX), and into the SpApp, when present, through sarco/endoplasmic reticulum Ca^{2+}-ATPase (SERCA) (Bell et al., 2019). We consider the spine as an isolated geometric compartment and do not consider the effect of calcium influx from the dendrite at this time scale. The base of the spine neck has a Dirichlet boundary condition of calcium clamped to zero and acts as a calcium sink, which represents Ca^{2+} leaving the spine into the dendrite owing to the sudden increase in calcium in the spine (Holcman et al., 2005).

• **Buffers:** We do not model the different buffer species but rather use a lumped parameter approach as was done before (Mahajan and Nadkarni, 2019; Bell et al., 2019). Because free Ca^{2+} is rapidly buffered in cells, we consider both mobile buffers in the cytoplasm and immobile buffers on the PM (Bell et al., 2019; Schmidt and Eilers, 2009; Schmidt, 2012). We also include an exponential decay of calcium throughout the cytoplasm to capture the complex cytosolic buffering dynamics without including explicit buffers. Addition of more species introduces many more free parameters and can make the model computationally intractable; therefore, we focus on a lumped parameter approach.

• **Stochastic trials:** Each simulation condition was run with 50 random seeds, and these individual runs were averaged to obtain mean and SD (Friedhoff et al., 2021; Bartol et al., 2015).

• **Model readouts:** We report Ca^{2+} dynamics in terms of the number of ions rather than concentration. This is because the total number of ions in the spine reflects total signal coming into the spine and is the natural output from these particle-based simulations. The total number of calcium ions is used as input to calculate the synaptic weight change.

• **Synaptic weight:** The synaptic plasticity model developed by Shouval et al. (2002) was adapted to have dependence on total calcium ions rather than calcium concentration. The rate of synaptic weight update depends on a learning rate, τ_w, and a thresholding function, Ω_w, that are both dependent on calcium ion levels (Fig. 1, c and d). The learning rate determines the rate of synaptic weight change, while Ω_w determines if the weight increases or decreases. Thresholds for LTP and LTD, θ_P and θ_D, are set so that an intermediate level of calcium leads to a weakening of a synapse and LTD, while an elevated level of calcium leads to the strengthening of a synapse and LTP (Shouval et al., 2002; Cho et al., 2001; Cormier et al., 2001).

Dynamics of calcium ions in the spine volume

We summarize the main reactions for Ca^{2+} in the volume. These reaction models were obtained from Bartol et al. (2015) and Bell et al. (2019) and are discussed in detail below. Model parameters are given in Table 2. We found that our calcium dynamics are comparable to previously published models (Bell et al., 2019; Bartol et al., 2015; Rubin et al., 2005; Hu et al., 2018) and

experimental observations (Sabatini et al., 2002; Hoogland and Saggau, 2004; Segal and Korkotian, 2014; Fig. S8).

In the volume, calcium binds with fixed and mobile buffers in the cytoplasm, modeled here generically by B_m to represent mobile calcium buffers and B_f to represent fixed buffers. Calcium-buffer binding is modeled by

$$Ca^{2+} + B_f \underset{k_{Bf,off}}{\overset{k_{Bf,on}}{\rightleftharpoons}} Ca \cdot B_f, \quad (1)$$

and

$$Ca^{2+} + B_m \underset{k_{Bm,off}}{\overset{k_{Bm,on}}{\rightleftharpoons}} Ca \cdot B_m. \quad (2)$$

Reaction rates for mobile and fixed buffers are provided in Table 2.

An additional Ca^{2+} decay term is given by

$$Ca^{2+} \overset{k_d}{\rightarrow} \emptyset, \quad (3)$$

where k_d sets the decay rate. The value of k_d is taken as 50 s^{-1} inspired by Bell et al. (2019) and Cugno et al. (2019).

PM

The primary influx of calcium through the PM occurs through NMDARs and VSCCs, and calcium is pumped out of the volume through PMCA and NCX. In this model, NMDARs depend on both voltage and glutamate and are localized to the PSD region. VSCCs are voltage dependent and localized throughout the PM. PMCA and NCX are calcium-dependent pumps and are also located throughout the PM surface.

NMDARs

NMDARs are localized to the PSD area with a surface density of 150 molecule μm^{-2} (Bartol et al., 2015). The activation of NMDAR is modeled with an asymmetric trapping block kinetic scheme as proposed in Vargas-Caballero and Robinson (2004). The activation of NMDAR depends on the diffusion of glutamate through the synaptic cleft and its binding to inactive receptors. A surface identical to the top of the spine head is translated 2 μm above the head to represent the synaptic cleft. At time $t = 0$ in each simulation, 500 molecules of glutamate are released at the center of this synaptic cleft. The released glutamate molecules diffuse through the cleft at a rate of 2.2×10^{-6} cm^2 s^{-1} and bind to membrane-bound proteins. On the postsynaptic membrane, NMDARs compete with the glutamate receptor AMPAR for glutamate; thus, AMPARs are also included in the simulation to model this competition, but do not play a role in calcium influx. AMPAR is also localized to the PSD area at a density of 1,200 molecule μm^{-2} (Bartol et al., 2015). The binding of glutamate to AMPAR is modeled according to the kinetic scheme proposed in Jonas et al. (1993).

Calcium ion flux through open NMDARs is modeled by the simple unimolecular reaction

$$NMDAR \overset{k_{Ca}}{\rightarrow} NMDAR + Ca^{2+}_{cyto}. \quad (4)$$

The rate of calcium influx is given by

$$k_{Ca}(V) = \gamma NMDAR \cdot \frac{V - V_\tau}{2 \cdot 1.6 \times 10^{-19}}, \quad (5)$$

where V is the membrane potential and V_r is the reversal potential of NMDAR. The parameters for the NMDAR reactions are the same as given in Vargas-Caballero and Robinson (2004), and the parameters for the AMPAR reactions are the same as those in Jonas et al. (1993).

Calcium influx through VSCCs

The influx of Ca^{2+} through an open VSCC is given by the reaction

$$\text{VSCC} \overset{k_{VSCC}}{\rightarrow} \text{VSCC} + Ca^{2+}_{cyto}. \quad (6)$$

The rate of calcium influx is given by

$$k_{VSCC} = \frac{\gamma V(t) N_A \left[0.393 - \exp\left(\frac{-V(t)}{80.36}\right)\right]}{2F\left[1 - \exp\left(\frac{V(t)}{80.36}\right)\right]} \quad (7)$$

The influx of Ca^{2+} through VSCCs is also dependent on the activation kinetics of VSCCs. The initial conditions for all the VSCCs is the closed state, and the activation of the channels is modeled here with a five-state kinetic scheme as used in Bartol et al. (2015). The parameters for Ca^{2+} influx through VSCCs are the same as in Bartol et al. (2015). VSCCs are located on the PM with a density of 2 molecules μm^{-2}.

Voltage calculations in the model

Because the transmembrane potential varies with time (Fig. 1 a, inset) and the rate constants for NMDAR and VSCC are voltage dependent, the values of these rate constants at each simulation step were precomputed and passed into MCell. The voltage stimulus representing a single EPSP starting at time $t = 0$, followed by a single BPAP occurring at an offset of 10 ms, was obtained from Bartol et al. (2015). Note that this time offset is within the typical window for spike timing–dependent plasticity (STDP) to induce LTP (Bartol et al., 2015; Griffith et al., 2016).

PMCA and NCX dynamics

PMCA and NCX are located on the PM with areal density 998 and 142 molecule μm^{-2}, respectively (Bartol et al., 2015), forcing calcium to flow out of the cell. These pumps are modeled using the set of elementary reactions and reaction rates from Bartol et al. (2015).

SpApp

Calcium enters the SpApp via SERCA pumps and leaks out. SERCA pumps are calcium dependent and located throughout the SpApp membrane at 1,000 molecules μm^{-2} (Bartol et al., 2015). SERCA influx is modeled as a series of elementary reactions with rates from Bartol et al. (2015). Calcium leakage from the SpApp into the cytosol is modeled by the reaction

$$Ca^{2+}_{ER} \overset{k_{leak}}{\rightarrow} Ca^{2+}_{cyto}, \quad (8)$$

where k_{leak} is 0.1608 s^{-1} from Bell et al. (2019).

Extracellular calcium

Extracellular calcium was not explicitly modeled for ease of computational tractability. We assumed a constant extracellular calcium concentration (2 mM) that is negligibly impacted by calcium influx to and efflux from the spine cytoplasm. The dynamics of Ca^{2+} are explicitly modeled once they enter the cell through channels located on the PM and cease to be explicitly represented once they are pumped out of the cell.

Synaptic weight change

Synaptic weight update was calculated using the classic model from Shouval et al. (2002). The governing equations were modified to take total number of Ca^{2+} ions rather than a concentration. Here, we use total number of ions to highlight the details available from a stochastic simulation and to consider the consequences of using this global readout on synaptic weight.

We modeled the changes in synaptic weight, w, as a phenomenological relationship, inspired by Mahajan and Nadkarni (2019) and Shouval et al. (2002). In our model, the change in synaptic weight is given by

$$\frac{dw}{dt} = \frac{\Omega_w - w}{\tau_w}, \tag{9}$$

where τ_w is a learning rate, given as

$$\tau_w = k_1 + \frac{k_2}{k_3 + 2Ca^{2+}_{cyto}(t) \Big/ (\theta_D + \theta_P)}, \tag{10}$$

and Ω_w describes calcium dependence in the regimes of LTP and LTD as

$$\Omega_w = \frac{1}{1 + exp\left\{-\beta_P\left[Ca^{2+}_{cyto}(t) - \theta_P\right]\right\}} - \frac{0.5}{1 + exp\left\{-\beta_D\left[Ca^{2+}_{cyto}(t) - \theta_D\right]\right\}} \tag{11}$$

We note that cytosolic calcium, $Ca^{2+}(t)$, is the total number of ions in the spine. The differential equation for synaptic weight, w, is solved in Matlab v2018b using ode23s, for each calcium transient predicted by the MCell model. The initial synaptic weight value is set to 0, so the change in synaptic weight and synaptic weight update are the same value for this single stimulation event. Synaptic weight parameters are given in Table 3.

Simulation information and parameters

Calcium simulations were conducted for a total simulation time of 35 ms with a 500 ns time step. Each geometry is simulated in MCell with 50 distinct seeds to generate an appropriate sample size of results. All simulations use a write-out frequency of once per iteration for reproducibility of results. Longer write-out frequencies introduce nondeterminism to the trajectories arising from the MCell reaction scheduler. At the beginning of each simulation, membrane proteins are randomly distributed over specified regions of the spine geometry surface area according to an assigned count or concentration. System configuration and analysis scripts are all available on Github (https://github.com/RangamaniLabUCSD/StochasticSpineSimulations).

Table 3. **Parameters for synaptic weight**

Variable	Value	Units	Reference
Initial w	0		Mahajan and Nadkarni (2019)
k_1	1	s	Mahajan and Nadkarni (2019)
k_2	10	s	Mahajan and Nadkarni (2019)
k_3	1×10^{-3}		Mahajan and Nadkarni (2019)
θ_D	100	Molecule	Mahajan and Nadkarni (2019);[a] Shouval et al. (2002)
θ_P	400	Molecule	Mahajan and Nadkarni (2019);[a] Shouval et al. (2002)
β_D	0.2977	Molecule^{-1}	Mahajan and Nadkarni (2019);[a] Shouval et al. (2002)
β_P	0.2977	Molecule^{-1}	Mahajan and Nadkarni (2019);[a] Shouval et al. (2002)

[a]These parameters were converted from concentration units with adjustments for consistency.

Online supplemental material

Fig. S1 presents the profiles of the idealized geometries used and various geometric parameters. Fig. S2 provides an artificial calcium input to demonstrate how the synaptic weight function depends on calcium transient dynamics. Figs. S3 and S4 provide additional plots of calcium transient dynamics against volume and as concentration in temporal plots, respectively. Figs. S5, S6, and S7 provide additional plots of the thin spine neck variations, mushroom spine neck variations, and thin spine with SpApp variations, respectively. Figs. S8 and S9 also compare our results to previous calcium transients and calcium dynamics, respectively. Figs. S10 and S11 compare the use of total ion number versus concentration to determine synaptic weight. Fig. S12 provides a matrix of two-tailed t tests between all simulations, and Fig. S13 provides synaptic weight predictions for a pulse train. Videos 1, 2, 3, 4, 5, 6, 7, 8, 9, and 10 show the spatiotemporal calcium dynamics. Table S1 and Table S2 list all geometric variations. Table S3 lists values for realistic geometries. Details on how to use realistic geometries in these simulation modalities can be found in the supplemental text at the end of the PDF.

Results

We first demonstrate the coupling between stochastic dynamics of calcium in a single spine to the deterministic model of synaptic weight update (Fig. 2). We then investigate whether spine size has any effect on synaptic weight change of filopodia-shaped spines (Fig. 3), thin spines (Fig. 4), and mushroom-shaped spines (Fig. 5). Next, we consider the role of the SpApp (Fig. 6). Finally, we investigate the relationship between spine morphology and synaptic weight update in realistic geometries (Fig. 7). Our results predict that synaptic weight change through calcium dynamics is a deterministic function of geometric parameters of the spines (Fig. 8). We discuss these results in detail below.

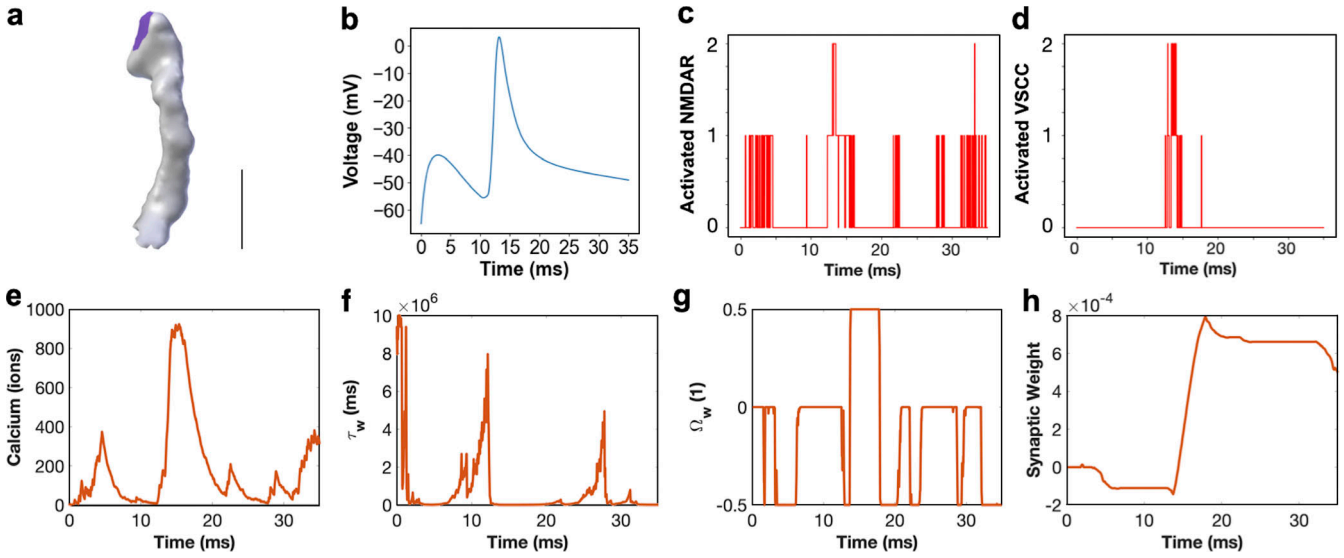

Figure 2. **Stochastic receptor, channel, and calcium dynamics inform deterministic synaptic weight update. (a)** A realistic thin spine with a volume of 0.045 μm^3 serves as an example spine to consider how stochastic receptor and channel dynamics translate into calcium transients that inform synaptic weight update. Scale bar, 0.5 μm. **(b)** The model stimulus includes a set voltage profile that activates both NMDARs and VSCCs. We considered a single seed run (seed 1 for the realistic thin spine 39). **(c)** Activated, open NMDARs over time for a single simulation in the realistic geometry shown in a. **(d)** Activated, open VSCCs over time for a single simulation in the realistic geometry shown in a. **(e)** Calcium transient due to the channel and receptor dynamics shown in c and d. **(f–h)** Learning rate τw (f), Ωw (g), and synaptic weight update (h) calculated from the calcium transient in e.

The coupled model filters stochastic Ca^{2+} dynamics to update synaptic weight

We demonstrate how the stochastic calcium model informs the deterministic synaptic weight predictions. We consider a single-seed trial for a single geometry, in this case seed 1 from a realistic thin spine (Fig. 2 a). We observed that in response to the voltage trace and glutamate release (Fig. 2 b), the NMDARs and VSCCs stochastically opened and closed (Fig. 2, c and d), resulting in a noisy calcium transient (Fig. 2 e). We compared our calcium transients to both published experimental (Sabatini et al., 2002; Hoogland and Saggau, 2004; Segal and Korkotian, 2014) and computational (Bell et al., 2019; Bartol et al., 2015; Rubin et al., 2005; Hu et al., 2018) results, and found a reasonable agreement (Fig. S8). We next calculated the learning rate (Fig. 2 f) and Ω_w (Fig. 2 g) terms in the synaptic weight model as a function of this calcium transient. We noticed that the noisy calcium dynamics were filtered into a smoother synaptic weight prediction (Fig. 2 h). For another example of how calcium pulse magnitude and width translates to synaptic weight update, see Fig. S2. With this understanding of how the two models integrate, we next investigated how spine geometry influences calcium transients and subsequent synaptic weight predictions.

Synaptic weight change depends on spine volume-to-surface-area ratio in filopodia-shaped spines

We began our analysis with a simple question: does spine size alter synaptic weight change? To answer this question, we first examined filopodia-shaped spines. Dendritic filopodia are precursors of dendritic spines and serve to bridge the gap between the dendrite and an axon that is passing by during synapse formation (Ozcan, 2017). These are highly motile, elongated structures that resemble tubules (lengths of 2–20 μm and neck diameters <0.3 μm). The simplicity of this geometry allows us to focus on the role of size alone in a simple spine geometry. We used spine geometries of three different volumes (0.017, 0.058, and 0.138 μm^3). Simulations revealed that the calcium dynamics in these tubule-shaped spines appeared to follow a "plug-flow" behavior in which, at 15 ms, all the calcium was localized to one region (Fig. 3 a). This behavior is because of the narrow geometry of the spine, preventing dispersion of the calcium (see also Video 1). Next, we examined the temporal dynamics of calcium and noted that the larger spines had larger numbers of calcium ions (Fig. 3 b) but also a larger variance of calcium ions (Fig. 3 c). We further characterized the dynamics by considering the peak calcium values and decay time constants of the calcium transients versus the spine volume-to-surface-area ratio. We chose the volume-to-surface-area ratio as a geometric metric of spine morphology because it encompasses both the cytosolic volume through which calcium diffuses and the surface area of the spine membrane through which calcium can enter and leave the system. Additional analyses with respect to spine volume are shown in Fig. S3 and example calcium transients are shown in Fig. S4.

We noted that, indeed, increasing spine size, and therefore the volume-to-surface-area ratio, causes a linearly proportional and significant increase in peak calcium ions (Fig. 3 d). We also found that the decay time of calcium from the peak decreased with increasing volume-to-surface-area ratios and satisfied an exponential dependence (Fig. 3 e). As spine size increases, the decay time constant decreases, showing that it takes longer for calcium to clear out of larger spines and spines with larger volume-to-surface-area ratios. Finally, we calculated the synaptic weight change (see Synaptic weight change) and compared this value at 35 ms across volume-to-surface-

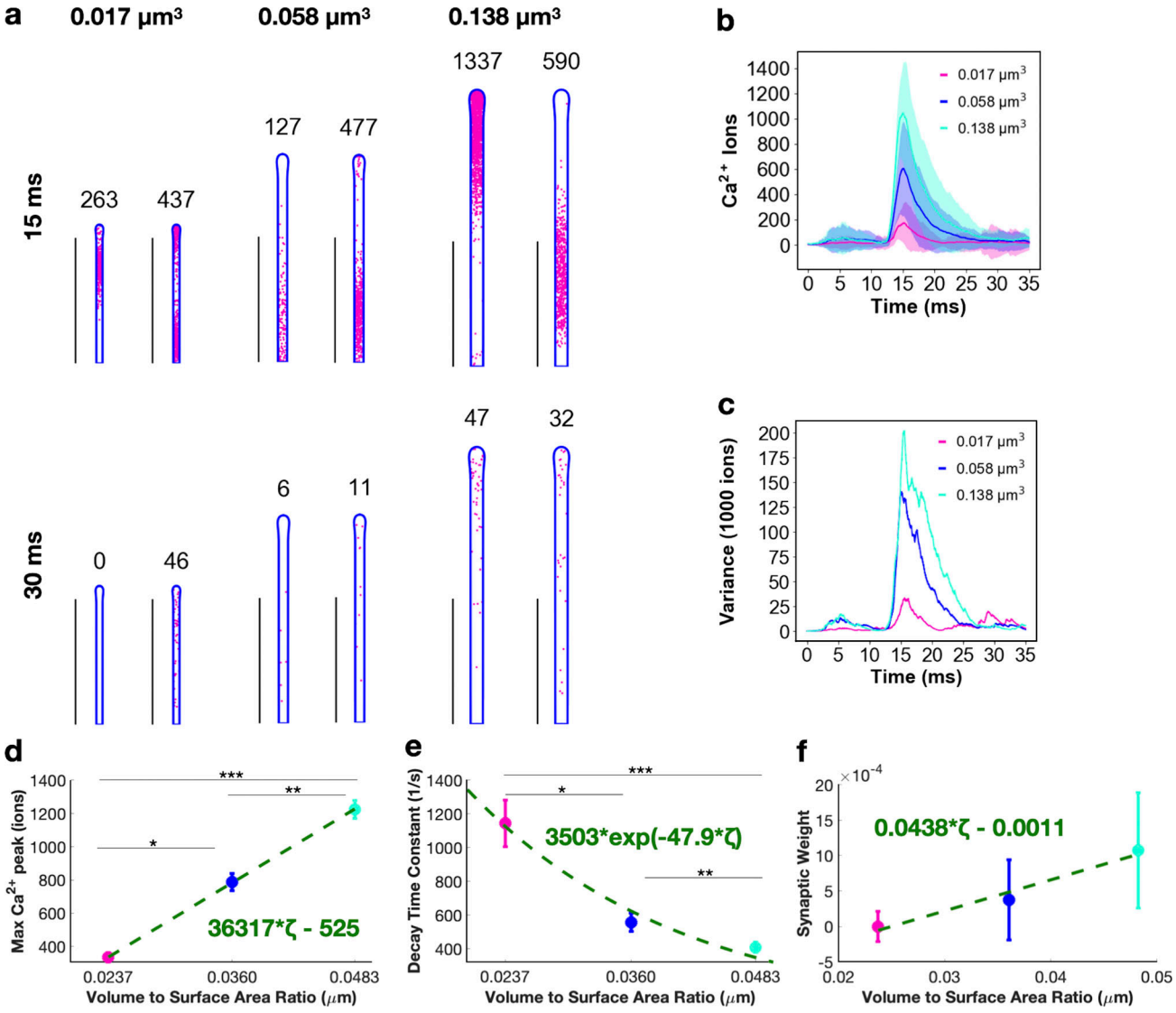

Figure 3. **Calcium dynamics and synaptic weight change in filopodia-shaped spines depend on spine volume-to-surface ratio. (a)** Spatial plots illustrating Ca^{2+} localization at 15 and 30 ms for filopodia-shaped spines with different volumes (0.017, 0.058, and 0.138 µm³). The number above each geometry corresponds to the number of Ca^{2+} in that frame. Two random seeds are shown as examples for each geometry. Scale bars, 2 µm. **(b)** Mean (solid) and SD (shaded area) of Ca^{2+} transients across 50 simulations for each of the three filopodia-shaped spine sizes. **(c)** Variance of Ca^{2+} over time, displayed as variance divided by 1,000 ions. **(d)** The mean and SEM (n = 50) of the peak number of Ca^{2+} in different filopodia-shaped spine sizes shows statistically significant differences; *, P = 2.0262 × 10^{-11}; **, P = 9.898 × 10^{-8}; ***, P = 4.362 10^{-26} using two-tailed t-test. We fitted the trend in peak Ca^{2+} as a linear function of volume-to-surface-area ratio, ζ; r^2 = 0.5521 for the linear fit. **(e)** The decay time scales of each Ca^{2+} transient were estimated by fitting with an exponential decay function $c\exp(kt)$. The mean and SEM (n = 50) of the decay time constant, k, shows statistically significant differences across filopodia-shaped spine sizes; *, P = 1.6331 × 10^{-4}; **, P = 0.0209; ***, P = 1.3381 × 10^{-6} from two-tailed t test. The mean decay time constants as a function of volume-to-surface-area ratio, ζ, were fitted with an exponential $a\exp(b\zeta)$; r^2 = 0.203 for the exponential fit. **(f)** The mean and SEM (n = 50) of the calculated synaptic weight change at the last time point in the simulation for all filopodia-shaped spine sizes, plotted against the volume-to-surface-area ratio, shows statistically significant differences between all cases; P_{12} = 2.7290 × 10^{-5}; P_{23} = 2.8626 × 10^{-6}; P_{13} = 1.6321 × 10^{-14} from two-tailed t test, where 1, 2, and 3 refer to the spines in increasing size. We fitted the trend in synaptic weight as a linear function of volume-to-surface-area ratio, ζ; r^2 = 0.3594 for the linear fit.

area ratios for the filopodia-shaped spines (Fig. 3 f). We observed that while the smallest spine had no observable weight change, presumably because of the net low calcium influx, the weight change increases with increase in spine volume-to-surface-area ratio (Fig. 3 f). Thus, we found that even for a shape as simple as a filopodia-shaped spine, changes in spine volume-to-surface-area ratio can dramatically alter calcium dynamics and synaptic weight change in stochastic conditions, suggesting a close coupling between spinogenesis and calcium handling.

Thin and mushroom spines modulate synaptic weight changes as a function of volume-to-surface-area ratio

We next asked whether the relationships of spine size and synaptic weight change observed for filopodia-shaped spines (Fig. 3) also held for thin and mushroom-shaped spines. Thin

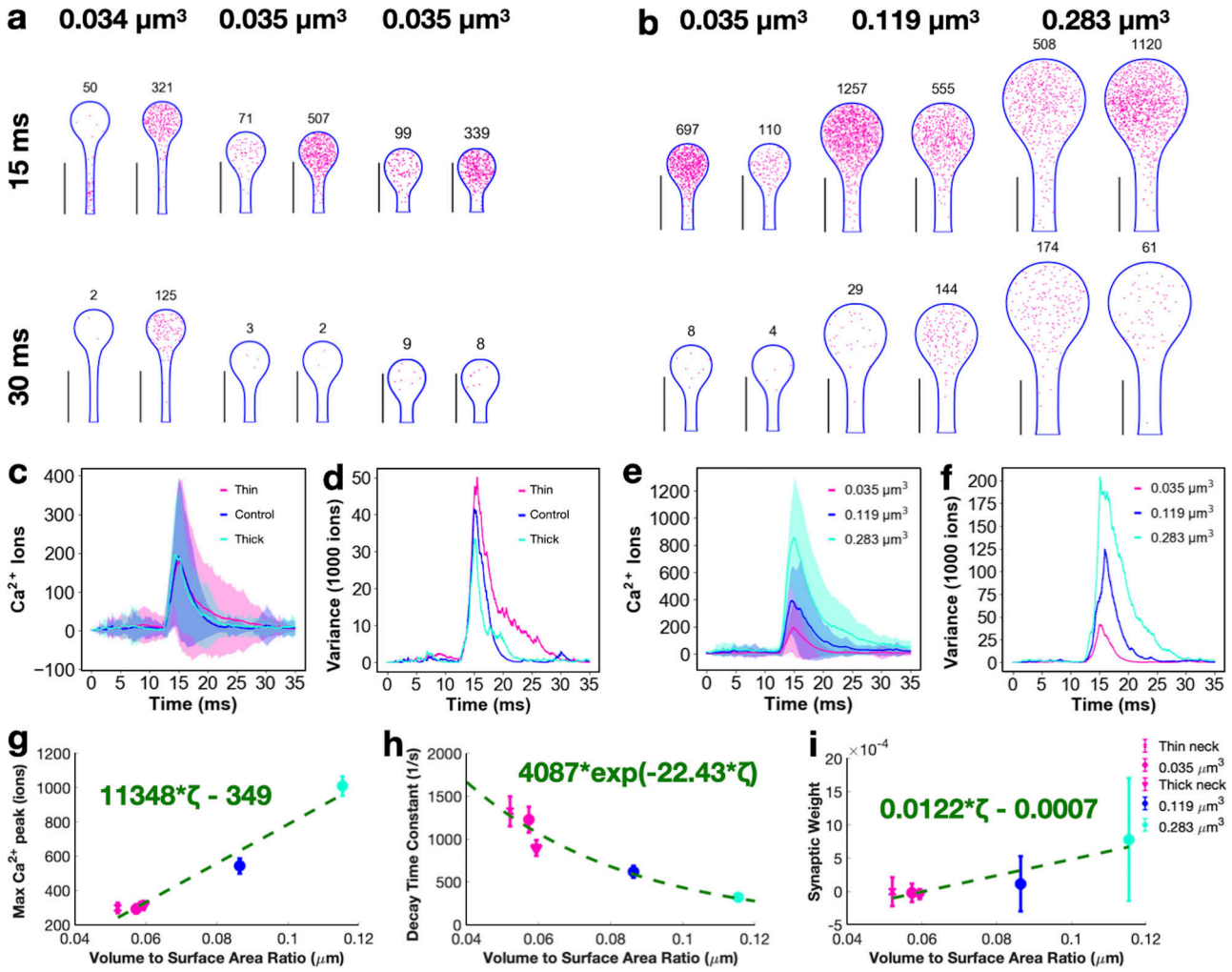

Figure 4. **Changing thin spine size modulates calcium dynamics and synaptic weight change. (a and b)** Spatial plots illustrating Ca^{2+} localization at 15 and 30 ms for small thin spines with three different neck lengths, 0.07, 0.06, and 0.04 µm (a) and three different volumes, 0.035, 0.119 and 0.283 µm³ (b). The number above each geometry corresponds to the number of Ca^{2+} ions in the frame. Two random seeds are shown as examples for each geometry. Scale bars, 0.5 µm. **(c)** Mean (solid) and SD (shaded area) of Ca^{2+} transients across 50 simulations for each of the three thin spines with different neck lengths. **(d)** Variance of Ca^{2+} over time for the thin spines with different neck lengths, displayed as variance divided by 1,000 ions. **(e)** Mean (solid) and SD (shaded area) of Ca^{2+} transients across 50 simulations for each of the three thin spine sizes. **(f)** Variance of Ca^{2+} over time for the thin spines of different sizes, displayed as variance divided by 1,000 ions. **(g)** The mean and SEM (n = 50) of the peak number of Ca^{2+} in different thin spine sizes and with different neck lengths show an overall increasing trend. The spines of different sizes show statistically significant differences between the each size; $P_{12} = 5.2641 \times 10^{-6}$; $P_{23} = 2.7377 \times 10^{-9}$; $P_{13} = 5.0036 \times 10^{-20}$ from two-tailed t test, where 1, 2, and 3 denote the different sized spines in increasing size. We fitted the trend in peak Ca^{2+} as a linear function of volume-to-surface-area ratio, ζ; $r^2 = 0.4939$ for the linear fit. **(h)** The decay time scales of each Ca^{2+} transient were estimated by fitting with an exponential decay function $c \exp(kt)$. The mean and SEM (n = 50) of the decay time constant, k, shows statistically significant differences across thin spine sizes; $P_{12} = 4.3976 \times 10^{-4}$; $P_{23} = 1.1541 \times 10^{-4}$; $P_{13} = 5.4590 \times 10^{-8}$ from two-tailed t test, where 1, 2, and 3 denote the different sized spines in increasing size. The mean decay time constants as a function of volume-to-surface-area ratio, ζ, were fitted with an exponential $a \exp(b\zeta)$; $r^2 = 0.1630$ for the exponential fit. **(i)** The mean and SEM (n = 50) of the calculated synaptic weight change at the last time point in the simulation for all thin spine sizes and neck lengths show an increasing trend against the volume-to-surface-area ratio. We fitted the trend in synaptic weight increase as a linear function of volume-to-surface-area ratio, ζ; $r^2 = 0.2698$ for the linear fit. The spines of different sizes show statistically significant differences between all sizes; $P_{12} = 0.0315$; $P_{23} = 1.0661 \times 10^{-5}$; $P_{13} = 2.5751 \times 10^{-8}$ from two-tailed t test, where 1, 2, and 3 denote the different sized spines in increasing size. Inset to right of i: legend for g–i.

and mushroom-shaped spines emerge from filopodia-shaped spines as spinogenesis progresses (Ozcan, 2017; Freire, 2010). It has been proposed that spines exist in a continuum of shapes (Ofer et al., 2021), but historically it has been useful to categorize spines into specific categories of shapes (Yuste, 2010). Thin spines, with small heads and thin necks, have been classified as "write-enabled" or learning spines due to their high motility. Mushroom spines, on the other hand, with bulbous heads and relatively wider necks, are termed "write-protected" or memory spines due to their stability (Jasinska et al., 2019). Thin spines are characterized by a spherical head, and we repeated the calcium influx simulations in a small thin spine with three different spine neck lengths (0.07, 0.06, and 0.04 µm) and thin spines of three different volumes (0.035, 0.119, and 0.283 µm³) that were informed by the ranges found in the literature (Fig. 4). We observed that, in thin spines, the

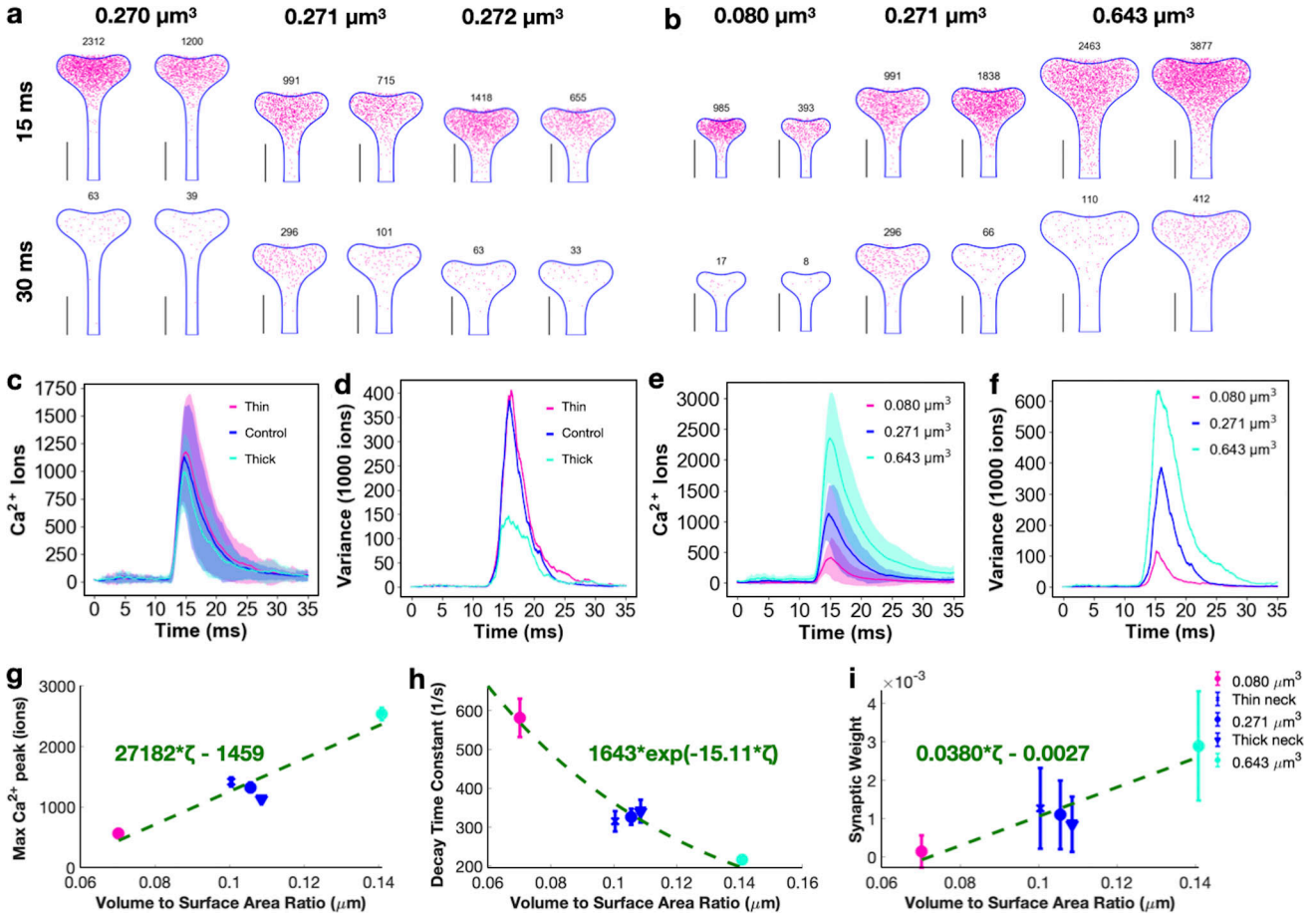

Figure 5. **Changing mushroom spine size modulates calcium dynamics and synaptic weight change. (a and b)** Spatial plots illustrating Ca^{2+} localization at 15 and 30 ms for medium mushroom spines with three different neck lengths, 0.13, 0.10, and 0.08 µm (a) and three different volumes, 0.080, 0.271, and 0.643 $µm^3$ (b). The number above each geometry corresponds to the number of Ca^{2+} in the frame. Two random seeds are shown as examples for each geometry. Scale bars, 0.5 µm. **(c)** Mean (solid) and SD (shaded area) of Ca^{2+} transients across 50 simulations for each of the three mushroom spines with different neck lengths. **(d)** Variance of Ca^{2+} over time for the mushroom spines with different neck length, displayed as variance divided by 1,000 ions. **(e)** Mean (solid) and SD (shaded area) of Ca^{2+} transients across 50 simulations for each of the three mushroom spine sizes. **(f)** Variance of Ca^{2+} over time for the mushroom spines of different sizes, displayed as variance divided by 1,000 ions. **(g)** The mean and SEM (n = 50) of the peak number of Ca^{2+} in different mushroom spine sizes and with different neck lengths show an overall increasing trend. The spines of different sizes show statistically significant differences between the each size; $P_{12} = 4.1244 \times 10^{-13}$; $P_{23} = 6.6467 \times 10^{-15}$; $P_{13} = 7.8934 \times 10^{-32}$ from two-tailed t test, where 1, 2, and 3 denote the different sized spines in increasing size. We fitted the trend in peak Ca^{2+} as a linear function of volume-to-surface-area ratio, ζ; $r^2 = 0.5474$ for the linear fit. **(h)** The decay time scales of each Ca^{2+} transient were estimated by fitting with an exponential decay function $c \exp(kt)$. The mean and SEM (n = 50) of the decay time constant, k, shows statistically significant differences across mushroom spine sizes; $P_{12} = 6.8175 \times 10^{-6}$; $P_{23} = 6.4075 \times 10^{-6}$; $P_{13} = 1.1118 \times 10^{-10}$ from two-tailed t test, where 1, 2, and 3 denote the different sized spines in increasing size. The mean decay time constants as a function of volume-to-surface-area ratio, ζ, were fitted with an exponential $a \exp(b\zeta)$; $r^2 = 0.2380$ for the exponential fit. **(i)** The mean and SEM (n = 50) of the calculated synaptic weight change at the last time point in the simulation for all mushroom spine sizes and neck lengths show an increasing trend against the volume-to-surface-area ratio. We fitted the trend in synaptic weight increase as a linear function of volume-to-surface-area ratio, ζ; $r^2 = 0.4224$ for the linear fit. The spines of different sizes show statistically significant differences between all sizes; $P_{12} = 5.1012 \times 10^{-10}$; $P_{23} = 2.0097 \times 10^{-11}$; $P_{13} = 2.1447 \times 10^{-23}$ from two-tailed t-test, where 1, 2, and 3 denote the different sized spines in increasing size. Inset to right of i: legend for g–i.

calcium ions were concentrated in the head at 15 ms but dispersed more uniformly by 30 ms (Fig. 4, a and b; and Video 2). We did not observe plug-flow-like behavior as we did for filopodia-shaped spines, likely because of the differences in both shape and volume of the thin spines. The thin spines with different neck lengths showed very similar calcium transients and variance (Fig. 4, c and d), except for the thin-necked spine, which showed much more variance during its decay dynamics. For a closer look at the thin spine neck variation dynamics, see Fig. S5.

Calcium dynamics in thin spines follows the expected temporal dynamics (Fig. 4 e), with larger spines having larger peak calcium and increased time to decay. Larger thin spines also have larger variance in calcium ion transients over time (Fig. 4 f). Next, we found that the maximum calcium ions per spine was significantly larger in larger spines, with statistically different values for the different-sized spines. The peak calcium increased linearly compared with spine volume-to-surface area but with a smaller slope compared with the filopodia-shaped spines (maximum peak values in filopodia-shaped spines

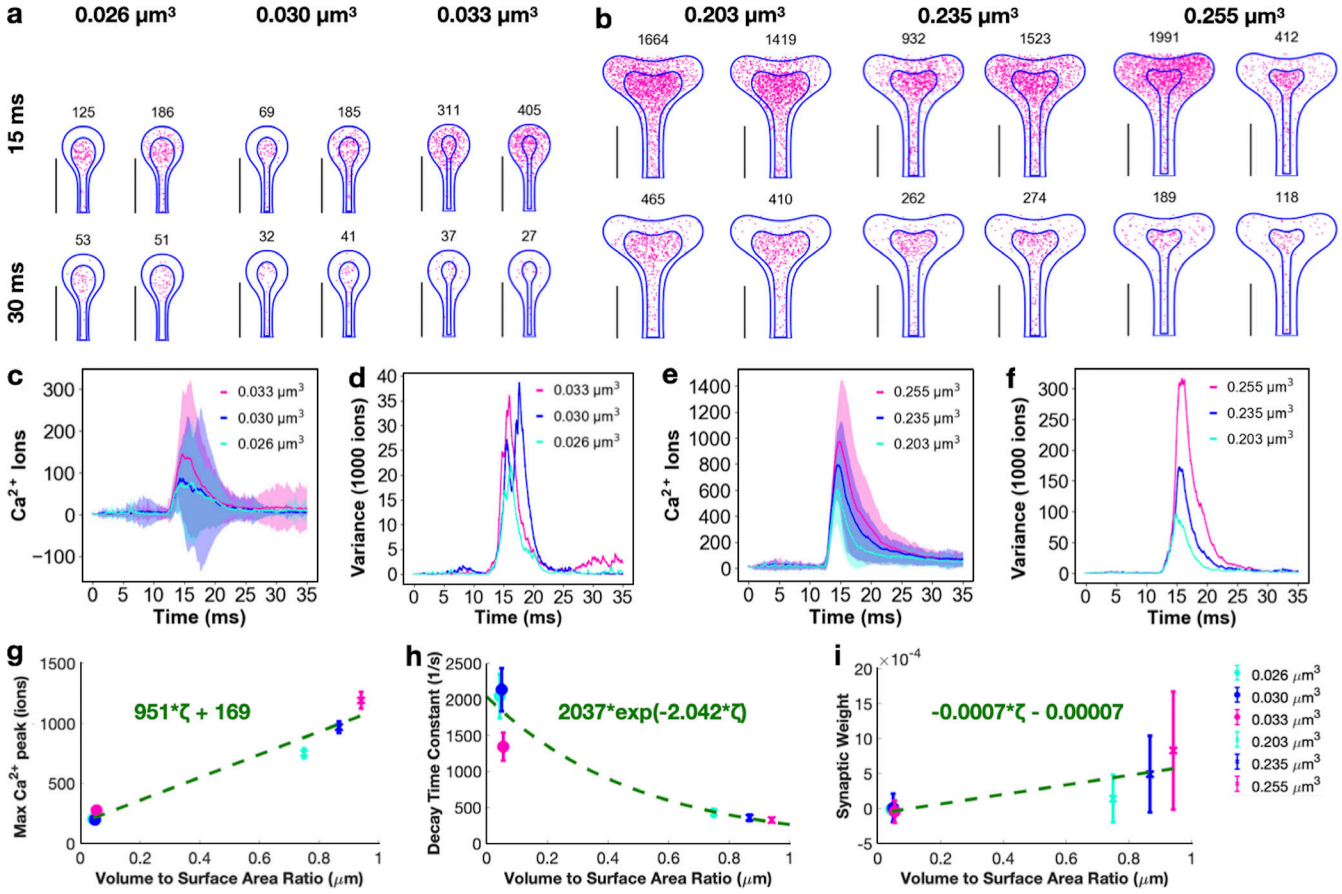

Figure 6. **Sp App size modulates synaptic weight change in mushroom spines. (a)** Spatial plots at 15 and 30 ms for thin spines with SpApp of different volumes (net spine volumes of 0.026, 0.030, and 0.033 μm³). **(b)** Spatial plots at 15 and 30 ms for mushroom spines with SpApp of different volumes (net spine volumes of 0.203, 0.235, and 0.255 μm³). The numbers on top of the shape indicate the total number of calcium ions at that instant in both the SpApp and cytoplasm. Two random seeds are shown as examples for each geometry. Scale bars, 0.5 μm. **(c and d)** Calcium ions over time as mean and SD (c) and variance, displayed as variance divided by 1,000 ions (d), for all three thin spines with different SpApp sizes. Shaded regions in c denote SD. **(e and f)** Calcium ions over time as mean and SD (e) and variance, displayed as variance divided by 1,000 ions (f), for all three mushroom spines with different SpApp sizes. Shaded regions in e denote SD. **(g)** Peak calcium ion number for each thin and mushroom spine with a SpApp, with the mean and SEM (n = 50), show an increasing trend over volume-to-surface-area ratio. We fitted the trend in peak values with a linear function against the volume-to-surface-area ratio, ζ; r^2 = 0.6091 for the linear fit. The mushroom spines show statistically significant differences between sizes; P_{12} = 0.0010; P_{23} = 0.0101; P_{13} = 4.0801 × 10^{-7} from two-tailed t test, where 1, 2, and 3 denote the different sized spines in increasing cytosolic volume. The thin spines show statistically significant differences only between two of the three paired cases; P_{13} = 0.0453; P_{23} = 0.0461 from two-tailed t test. **(h)** We fitted the decay dynamics of each calcium transient with (c exp[kt]) and report the decay time constant, k, as a mean and SEM (n = 50) against volume-to-surface-area ratio. The decay time constants were not statistically different for the mushroom spines, but the thin spines show a statistical difference between the second and third spine; P_{23} = 0.0289 from two-tailed t test. We fitted the trend in decay time constants as a function of volume-to-surface-area ratio with an exponential a exp($b\zeta$), where ζ is the volume-to-surface-area ratio; r^2 = 0.2219 for the fit. **(i)** Calculated synaptic weight change mean and SEM (n = 50) at the last time point for all three thin spines with SpApp and all three mushroom spines with SpApp show an increasing trend. We fitted the trend in synaptic weight with a linear function against the volume-to-surface-area ratio, ζ; r^2 = 0.2558 for the linear fit. Calculated synaptic weight change at the last time point for all three thin spines shows no statistically significant difference due to SpApp size. The mushroom spines had statistically significant differences between all cases; P_{12} = 2.0977 × 10^{-4}; P_{23} = 0.0198; P_{13} = 6.0097 × 10^{-7} from two-tailed t-test, where 1, 2, and 3 denote the different sized spines in increasing cytosolic volume. Inset to right of i: legend for g–i.

increased three times faster than those in thin spines; Fig. 4 g). This suggests that the size dependence of calcium grows slower in thin spines than in filopodia-shaped spines. The decay time also showed an exponential decay in thin spines with increasing volume-to-surface-area ratio (Fig. 4 h). The exponent was smaller for thin spines compared with filopodia-shaped spines (47.9 versus 22.43), suggesting that the decay rate with respect to volume-to-surface-area ratio was slower in thin spines. Finally, the synaptic weight change showed an increase with volume-to-surface-area ratio in thin spines (Fig. 4 i), indicating that larger spines are capable of stronger learning outcomes.

Finally, we repeated our analysis for mushroom-shaped spines of different neck length (0.13, 0.10, and 0.08 μm) and increasing volume (0.080, 0.271, and 0.643 μm³; Fig. 5). The effect of the shape of the spines is evident in the spatial dynamics of calcium (Fig. 5, a and b; and Video 3). Even at 15 ms, we noted that while a vast majority of calcium ions were localized in the spine head, there was spillover of calcium into the neck; this is particularly evident in the spines of larger volume

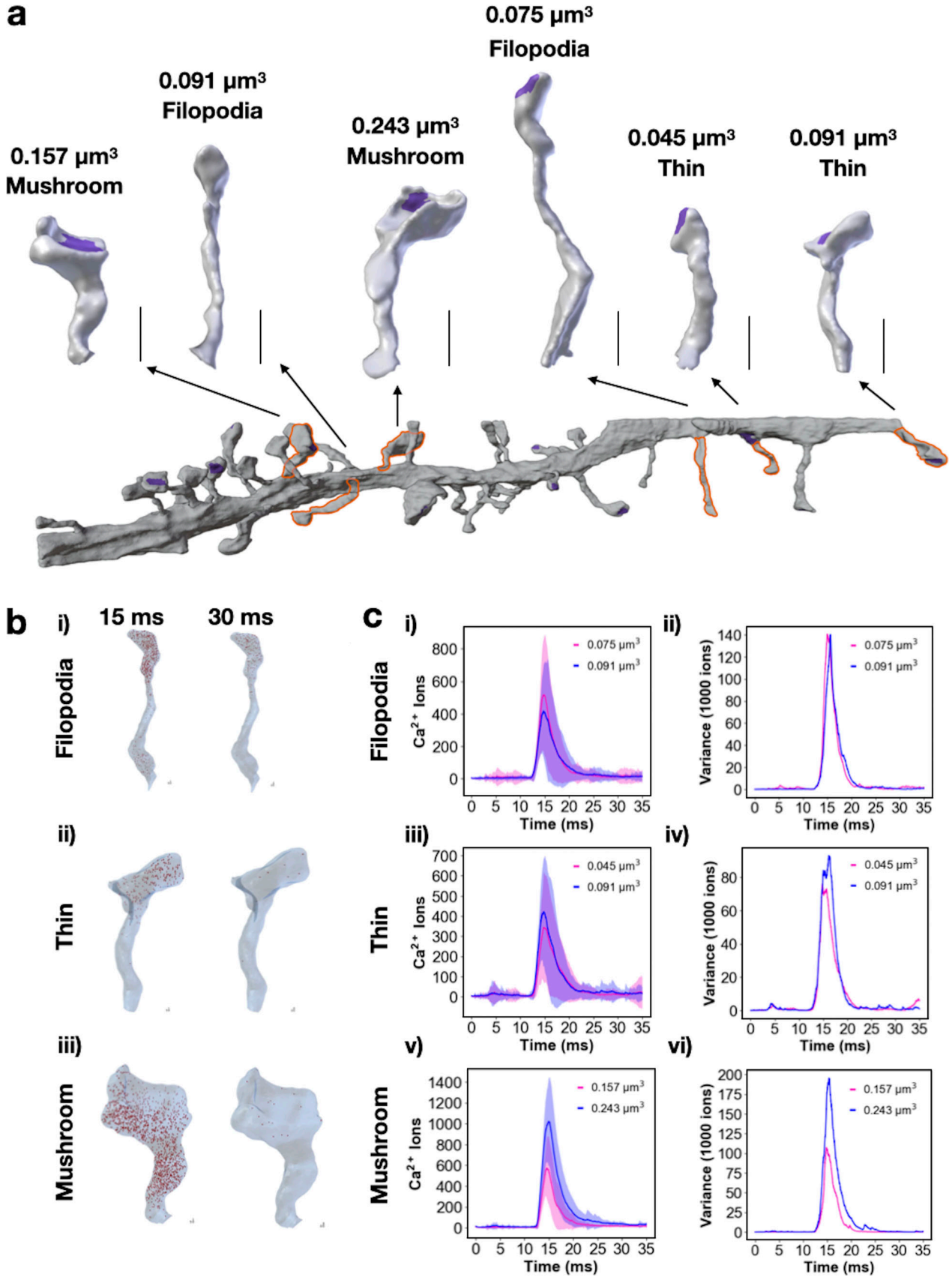

Figure 7. **Real spine geometries show size dependence for calcium dynamics. (a)** Spines similar to the idealized geometries were selected from a reconstructed dendrite (Wu et al., 2017). Representative filopodia-shaped spines, thin spines, and mushroom spines were selected and labeled with their volume

and shape. Scale bars, 0.5 µm. **(b)** Snapshots at 15 and 30 ms for a single seed for a filopodia-shaped spine (i), thin spine (ii), and mushroom spine (iii). **(c)** Calcium transients as means and SD, along with variance over time for the realistic spines of different shapes: (i and ii) filopodia-shaped spines, (iii and iv) thin spines, and (v and vi) mushroom spines. The realistic spines are labeled with their volumes.

(Fig. 5, a and b). Spine neck length showed similar increase and decay dynamics to each other (Fig. 5, c and d), but the thick-neck mushroom spine in particular showed a reduced variance. For a closer look at the mushroom spine neck variation dynamics, see Fig. S6. The effect of increases in volume, and therefore increases in volume-to-surface-area ratio, on the temporal dynamics of calcium is an increase in peak calcium (Fig. 5, e and g) and variance (Fig. 5 f) and a decrease in the decay time constant (Fig. 5 h). Interestingly, changing the neck length in the mushroom spine creates the opposite trend with respect to volume-to-surface-area ratio (Fig. 5, g and h), suggesting that spine neck length is an additional geometric factor for mushroom spines to tune their calcium response. The synaptic weight change in mushroom spines increases with spine volume-to-surface-area ratio and is larger for these mushroom spines than the filopodia-shaped and thin spines (Fig. 5 i). We observed that the peak calcium showed a linear increase with volume-to-surface-area ratio, with a slope that lies between the thin spines and filopodia-shaped spines. Finally, the decay time constant decreased with spine volume-to-surface-area ratio but with a smaller exponential decay compared with thin spines and filopodia-shaped spines. These two results point to the following conclusions. First, an increase in spine volume results in an increase in critical readouts of synaptic plasticity, and second, the shape of the spine alters the quantitative relationships of synaptic plasticity by allowing access to different volume-to-surface-area ratios.

SpApp size tunes synaptic weight changes by altering the volume-to-surface-area relationships

Approximately 14% of dendritic spines have specialized ER called SpApp, which are preferentially present in larger, mature spines (Chirillo et al., 2019; Spacek and Harris, 1997; Bell et al., 2019). Furthermore, recent studies have shown that the SpApp and the ER are dynamic structures in the dendrite and dendritic spines (Perez-Alvarez et al., 2020). Previously, we showed that the SpApp modulates calcium transients in deterministic models of calcium influx (Bell et al., 2019) by altering the net fluxes (Cugno et al., 2019). Here, we investigated how these relationships are altered in stochastic models in thin and mushroom spines (Fig. 6). When a SpApp is present in the spine head, it effectively reduces the volume of the spine cytosol and, in the time frame of our consideration, acts as a calcium sink (by the action of the SERCA pumps; Sabatini et al., 2002). One example trajectory in a mushroom spine with a SpApp is shown in Video 4. We varied SpApp size in the small-sized thin spine and medium-sized mushroom spine (Fig. 6, a and b; and Table S2). Calcium transients and variance showed much smoother dynamics for the mushroom spines than the thin spines (compare Fig. 6, e versus c). Peak calcium values were all statistically different for the different SpApp sizes in the mushroom spines but not the thin spines. Decay time constants were fitted with an exponential relationship (Fig. 6 h), but there were no statistical differences across different mushroom spines. All different sizes of the SpApp produce synaptic weight changes that are statistically different in the mushroom spines; increases in SpApp size result in smaller spine volume (and smaller volume-to-surface-area ratio) and therefore produce smaller weight changes (Fig. 6 i). The thin spines had a more complex trend and did not have statistically significant differences in predicted synaptic weight. For a closer look at the variations of the SpApp within thin spines, see Fig. S7. We conclude that the presence of SpApp alters the volume-to-surface-area ratio for spines and therefore tunes calcium levels and synaptic weight updates in the large mushroom spines with an inverse relationship to SpApp size.

Simulations in realistic geometries reveal that synaptic weight change depends on spine volume and volume-to-surface-area ratio

Thus far, we focused on idealized geometries of spines to identify relationships between key synaptic variables and key geometric variables. We found that the peak calcium value, decay time constant, and synaptic weight depend on the volume-to-surface-area ratio within each shape classification. Do these relationships hold for realistic geometries as well? To answer this question, we selected realistic geometries from mesh models (Lee and Laughlin, 2020) informed by electron micrographs from Wu et al. (2017).

Realistic spines have more complex geometries that do not fall into the exact morphological categories that we used for idealized spines. To test the significance of these variations, we selected two spines of each shape (thin, mushroom, and filopodia) and conducted simulations with the exact same parameters as the idealized simulations (Fig. 7 a). We chose realistic geometries that were within the range of sizes of the idealized geometries. The PSDs in the realistic spines were annotated during the segmentation process, and no modifications were made to the PSD marked regions. To capture filopodia-shaped protrusions, we selected long, thin spines (with minimal differentiation between the head and neck) that had marked PSD, because we did not include dendritic filopodia in the dendrite section. Details on how to use realistic geometries in these simulation modalities can be found in the supplemental text at the end of the PDF. We showed the spatial distribution of calcium ions for a single seed for filopodia, thin, and mushroom spines (Fig. 7 b) and found that due to the complexity of realistic morphologies, the calcium distribution was more complicated than those observed in the idealized spines.

For filopodia-shaped spines, we found that peak calcium and variance varied with volume, but the variance was not appreciably different for the two spines that we used to conduct simulations (Fig. 7, c i and ii; and Videos 5 and 6). The realistic thin spines we chose had volumes similar to the filopodia-shaped spines, and they also exhibited calcium dynamics

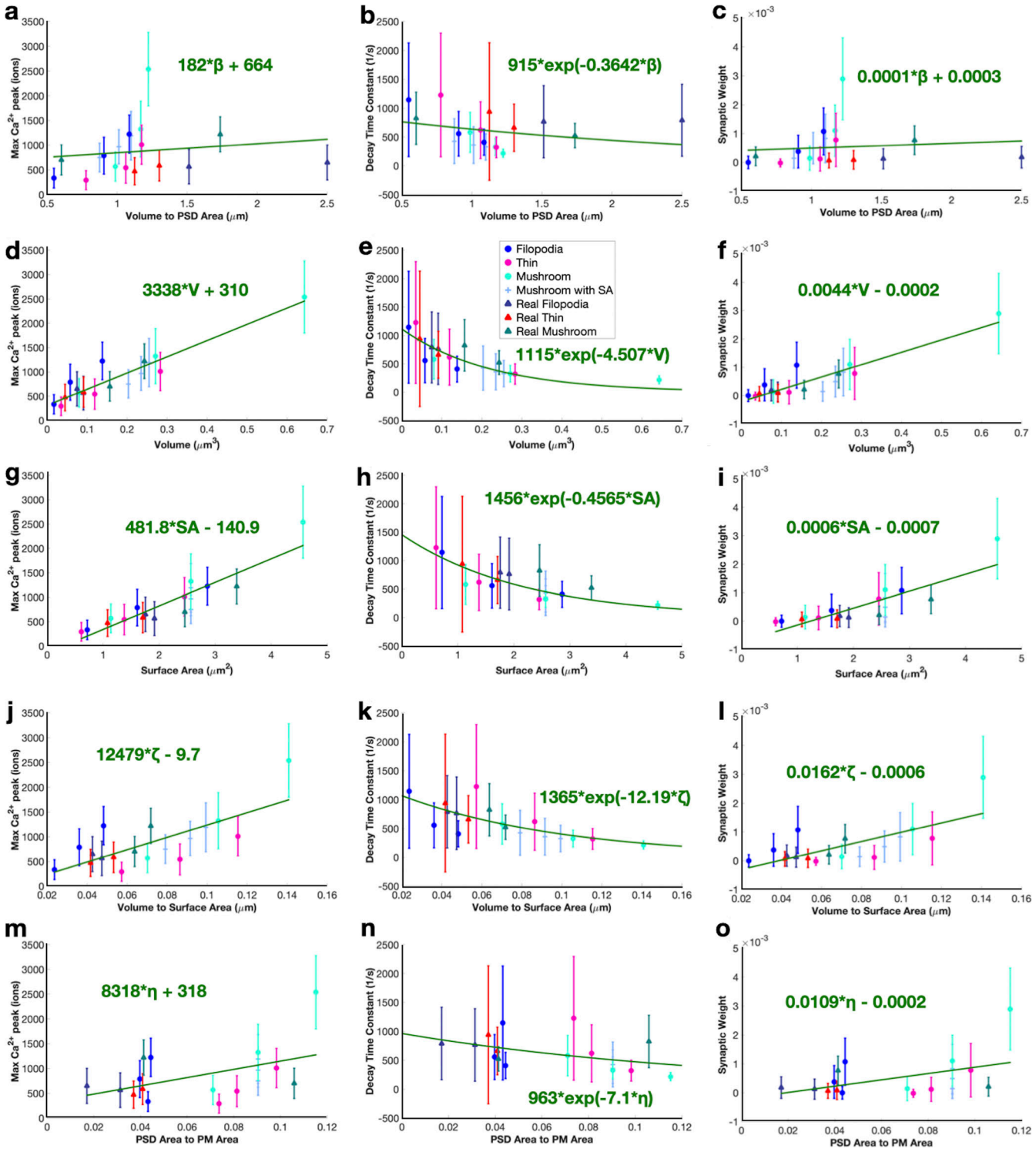

Figure 8. **Idealized and realistic spines show overall trends in peak calcium, decay rates, and synaptic weight change with respect to various geometric parameters.** We plotted all calcium peaks, decay time constants, and synaptic weight predictions for the various geometries against different geometric parameters including volume-to-PSD-area, volume, surface area, volume-to-surface-area ratio, and PSD-area-to-PM-area. We fitted the trends in peak values with a linear function against the geometric parameter. We fitted the decay dynamics of each calcium transient with $c\exp(kt)$ and report the decay time constant, k, as mean and SEM (n = 50) against the geometric parameter. We fitted the trend in synaptic weight change with a linear function against the geometric parameter. **(a)** All calcium peaks as mean and SEM (n = 50) across volume-to-PSD area ratio show no dependence. r^2 = 0.0152 for the linear fit. **(b)** r^2 = 0.0091 for the fit of decay time constants against volume-to-PSD area ratio. **(c)** Calculated synaptic weight change mean and SEM (n = 50) at the last time point for all idealized and realistic spines shows no dependence on volume-to-PSD area ratio. r^2 = 0.0060 for the linear fit. **(d)** All calcium peaks as mean and SEM (n = 50) across volume show a clear increasing trend. r^2 = 0.5666 for the linear fit. **(e)** r^2 = 0.1478 for the fit of decay time constants against volume. **(f)** Calculated synaptic weight change mean and SEM (n = 50) at the last time point for all idealized and realistic spines shows an increasing trend against

volume. r^2 = 0.4635 for the linear fit. **(g)** All calcium peaks as mean and SEM (n = 50) across surface area show a clear increasing trend. r^2 = 0.5327 for the linear fit. **(h)** r^2 = 0.1427 for the fit of decay time constants against surface area. **(i)** Calculated synaptic weight change mean and SEM (n = 50) at the last time point for all idealized and realistic spines shows an increasing trend against surface area. r^2 = 0.3887 for the linear fit. **(j)** All calcium peaks as mean and SEM (n = 50) across volume- to- surface- area ratio show an overall increasing trend. r^2 = 0.351 for the linear fit. **(k)** r^2 = 0.1114 for the fit of decay time constants against volume-to-surface-area ratio. **(l)** Calculated synaptic weight change mean and SEM (n = 50) at the last time point for all idealized and realistic spines shows an increasing trend against volume-to-surface- area ratio. r^2 = 0.2815 for the linear fit. **(m)** All calcium peaks as mean and SEM (n = 50) across PSD surface area to PM surface area ratio show an overall increasing trend. r^2 = 0.1441 for the linear fit. **(n)** r^2 = 0.0428 for the fit of decay time constants against PSD-to-surface-area ratio. **(o)** Calculated synaptic weight change mean and SEM (n = 50) at the last time point for all idealized and realistic spines shows an increasing trend against PSD-to-surface-area ratio. r^2 = 0.1186 for the linear fit. Inset above e: legend for all plots.

proportional to their volume (Fig. 7, c iii and iv; and Videos 7 and 8). Mushroom spines had larger volumes and larger PSD areas compared with thin or filopodia spines (Fig. 7, c v and vi; and Videos 9 and 10). Again, the calcium dynamics was proportional to the volume and showed that larger spines have higher peak calcium values. Thus, the relationships of spine geometry and calcium dynamics hold in realistic geometries as well.

Discussion

Dendritic spines have been extensively studied as biochemical signaling compartments, and their role in calcium sequestration has been theorized (Bell et al., 2019; Cugno et al., 2019; Yuste et al., 2000; Kotaleski and Blackwell, 2010; Murakoshi and Yasuda, 2012; Yasuda, 2017; Friedhoff et al., 2021). Their unique morphological traits and the classification of spine sizes and shapes with respect to function suggest possible structure–function relationships at the level of individual spines. In this work, we used stochastic modeling of calcium transients in dendritic spines of different geometries to understand how spine size and shape affect the change in synaptic weight. Using a stochastic simulation is important to investigate variance among spine shape and size, as dendritic spines have small volumes and probabilistic channel dynamics. Using idealized and realistic geometries, we found that geometric properties, specifically volume-to-surface-area ratio, affected key properties of calcium transients including peak calcium, decay time constants, and synaptic weight change. We discuss these findings in the context of different aspects of synaptic plasticity.

Our models predict that despite the individual calcium transients being stochastic, there is a predictive deterministic trend that appears to carry through the different sizes and shapes of the spines used in our model (Fig. 8). One of the advantages of our modeling approach here is that we can directly compare across the entire range of idealized and realistic geometries. By considering all the data from our models, for a total of 18 geometries with 50 simulations in each, we found that the peak calcium number is more or less linear with the volume, surface area, and volume-to-surface-area ratio (Fig. 8, d, g, and j). The decay time constant for calcium transients shows an exponential decay for larger volume-to-surface-area ratios, volumes, and surface areas, with quite a bit of variability for smaller ratios (Fig. 8, e, h, and k). We note that both peak calcium and decay time constants show clearer trends within the same spine protrusion type (i.e., comparing within the same color). Finally, the synaptic weight change increases as volume-to-surface-area ratio, volume, and surface area increase (Fig. 8, f, i, and l). We emphasize that our goal is to demonstrate a trend in the data as opposed to building numeric functions. Although we fitted the various data, the r^2 is often weak, indicative of the complexities that underlie such efforts.

We want to highlight two takeaways from the synaptic weight trends with respect to volume-to-surface-area ratio. The first takeaway is that within a spine shape group (comparing within a specific color in Fig. 8), there are clear increasing trends with respect to volume-to-surface-area ratio. The second takeaway is that while there are general trends in the data highlighted by the fit lines in Fig. 8, there appear to be three regions with slightly different synaptic weight trends at small, intermediate, and large volume-to-surface-area ratios. We discuss the possible consequences of these trends in more detail below.

In the idealized geometries, the PSD area is a manually fixed proportion of the spine volume, but realistic geometries do not have this artificial constraint. Therefore, we redid our analysis using volume to PSD area ratio and PSD area-to-surface-area ratios (PSD to PM ratio). Interestingly, we did not see a clear trend within the plots against volume to PSD area ratio (Fig. 8, a–c). In comparison, the PSD area to PM area ratio shows the same relationships overall as volume-to-surface-area ratio (Fig. 8, m–o), but this time with clustering of data around some ratios. This indicates that the PSD area is an important additional degree of freedom for synaptic weight change that must be considered for interpretation of geometric features, and using realistic geometries with boundary markings allows us to investigate this. It is important to note that there is a lot more variability in the smaller volume-to-surface-area ratios, suggesting that the response of smaller spines may be more variable than that of larger spines. This feature can work as a double-edged sword: it may provide an advantage during the development of spines or be an disadvantage in the case of loss of spines (Yuste and Bonhoeffer, 2004; Stein and Zito, 2019).

We interpret our predictions in the context of spine shapes. Filopodia are prevalent during early synaptogenesis and can transition into dendritic spines based on synaptic activity (Ozcan, 2017). Additionally, various disease states produce modified dendritic spines that appear more like filopodia (Ruhl et al., 2019). The lack of significant weight changes for the smallest filopodia-shaped spine indicates that there is a volume threshold at which filopodia receive enough stimulus to trigger synaptic weight change and transition toward more stable, mature dendritic spines. Importantly, the early synaptic weight changes emphasize how the increase in spine volume changes the weight outcome from LTD to LTP. This increase in synaptic

weight emphasizes how an increase in spine size can push a thin spine to transition into a stable, larger mushroom spine.

The difference in peak calcium level, decay dynamics, and synaptic weight changes as different spine shapes are scanned across different sizes can also provide insight into spine shape transitions during development and maturation. Filopodia-shaped spines have larger increases in peak calcium levels and synaptic weight updates and faster decreases in decay time constants as their volume-to-surface-area ratios and volumes increase, compared with both thin and mushroom spines (Figs. 3, 4, and 5). This suggests that filopodia spines can very quickly alter their calcium levels and therefore are well suited for initially identifying possible synaptic partners and subsequently directing resources to those filopodia that are good candidates to transition to dendritic spines (Lohmann and Bonhoeffer, 2008). Once filopodia are established, their linear calcium increase with volume might be unsustainable and might lead to reduced levels of increase for thin spines of comparable volume-to-surface area (and volume). This suggests that larger stimuli might be necessary to push thin spines toward more excitation, perhaps to prevent excessive numbers of thin spines from maturing and leading to resource depletion and excess neural connectivity (Sorra and Harris, 2000). Mushroom spines once again show more of an increase in synaptic weight as they increase in volume-to-surface-area ratio (and volume), but at volumes shifted from the filopodia-shaped spines, perhaps highlighting their role as key communication hubs (Sorra and Harris, 2000). The volume shift seen in mushroom spines versus filopodia-shaped spines might serve to limit the number of mature, highly excitable dendritic spines as both a key neuronal network and resource regulation feature. When the SpApp acts as a sink, its presence dampens synaptic weight changes in mushroom spines, potentially acting to stabilize the spine from future changes, as suggested by others (Jasinska et al., 2019; Mahajan and Nadkarni, 2019).

When considering why these trends hold across volume-to-surface-area ratios, it is important to note that Ca^{2+} influx is through receptors and channels with constant densities at the PM, or in the case of NMDARs, localized to the PSD. Therefore, as spines get larger, they have more surface area and more Ca^{2+} influx, which leads to higher numbers of total Ca^{2+} ions. This increase in total ions due to constant receptor and channel densities explains the increasing trend in peak Ca^{2+} number. When considering decay dynamics, Ca^{2+} efflux is due to pumps of constant density on the PM or the SpApp. Additionally, Ca^{2+} ions decay everywhere in the cytoplasm, bind to mobile buffers in the cytoplasm and fixed buffers on the PM, and bind to the spine neck base, which acts as a sink. Therefore, since many efflux or binding terms are either on the PM through pumps or at the base of the spine neck, larger volume-to-surface-area ratios mean that ions must diffuse further to reach the neck base or PM, explaining why decay time constants seem to decrease with increasing volume-to-surface-area ratio.

While changing geometric features can occur when spines increase and decrease in volume, they can also modify their volume, surface area, and volume-to-surface-area ratio by having a SpApp or through changes in spine neck geometry. We investigated these additional features (Figs. 4, 5, 6, S5, S6, and S7) and found that spine neck and SpApp size had volume-dependent effects. The smaller thin spine neck length and SpApp variations did not show much influence on peak calcium, decay rate, or synaptic weight, while the larger mushroom spine neck length and SpApp variations did have some impact on these readouts. Therefore, there are various means by which a spine can modify its synaptic weight response.

There has been substantial debate on deterministic versus stochastic studies for spine signaling (Kummer et al., 2005; Rüdiger, 2014; Skupin et al., 2010). Numerous studies have looked at the importance of stochastic calcium dynamics (Friedhoff et al., 2021; Friedhoff and Ramlow, 2021), and we agree that the consideration of stochasticity is important as noise often leads to efforts to average out its effects (Anwar et al., 2013). However, comparing our findings here to our previous deterministic results (Bell et al., 2019) shows that geometric factors play a critical role in determining Ca^{2+} dynamics; both approaches show that Ca^{2+} characteristics depend on the volume-to-surface-area ratio. Additionally, our hybrid approach of stochastic calcium dynamics and deterministic synaptic weight update is becoming increasingly common (Anwar et al., 2013; Rüdiger, 2014; Rodrigues et al., 2022 *Preprint*). However, care should still be taken in assuming model type as the dynamics of the species, not just particle number, plays an important role in the stochasticity of the system (Kummer et al., 2005).

We note that our study is only a small piece of the puzzle with respect to synaptic plasticity. There are many open questions remaining. Of particular interest and needing additional exploration is whether one should use total number of calcium ions or calcium concentration in evaluating synaptic weight change. For instance, we found that when calcium results are converted from total ions to average concentration along with the phenomenological synaptic weight equations, we got different trends in synaptic weight update results (Figs. S10 and S11). We note that this model of synaptic weight change has been used previously for concentration studies (Mahajan and Nadkarni, 2019; Shouval et al., 2002). We also observe that converting our previous results (Bell et al., 2019) into total ions shows the same trends for maximum Ca^{2+} peak and decay time constants as the current study (Fig. S9). Thus, a simple unit consideration can lead to conflicting results in spatial models and indicates that we need further discussion and investigation on the structure of phenomenological equations for synaptic weight to understand which factors of calcium dynamics matter and to what degree. Additional investigation is also needed in experimental data to relate fluorescence readouts to concentration or molecule numbers. However, we do compare our calcium transients to previously published experimental and computational results and find reasonable agreement (Fig. S8).

Related to these conflicting findings when considering ion total versus concentration, previous studies have considered the assumptions between calcium influx and spine geometry, more specifically the assumption of how calcium influx scales with spine volume (O'Donnell et al., 2011). Here the constant receptor and channel density assumption leads to an under-compensation

scenario in which calcium influx does not scale with spine volume, leading to lower calcium concentrations for larger spines. See Fig. S4 for examples of our model results in terms of calcium concentration. Because the synaptic weight model depends on calcium influx, when using concentration to determine synaptic weight, larger volume spines have less synaptic weight increase. Therefore, the sublinear calcium influx assumption leads to this discrepancy in synaptic weight predictions based on total calcium ions versus ion concentration. See Figs. S10 and S11 for examples of this discrepancy. Further research is needed to determine how exactly calcium influx scales with dendritic spine volume in vivo, as it is currently unknown which assumption is correct (O'Donnell et al., 2011). Regardless of the relationship between dendritic spine volume and calcium influx, the spine uses various means to modify its calcium transients, including internal organelles such as the SpApp acting as either a calcium source or sink (Matsuzaki, 2007). More research is needed to explore the relationship of geometry-dependent calcium trends and their consequences on phenomenological synaptic weight predictions.

An additional limitation of this study is the use of traditional P values for statistical analysis of the data (see Fig. S12 for details on *h* and P values), since the statistics field has suggested moving away from null-hypothesis significance testing (Wasserstein et al., 2019). We also note that our current focus is on very early events, and these models must be extended to longer-time-scale events to explore the biochemical and geometric interplay for downstream signaling (Bhalla, 2004; Ohadi and Rangamani, 2019; Ohadi et al., 2019; Mäki-Marttunen et al., 2020). Associated with these longer-time-scale events, calcium often occurs in pulse trains owing to high-frequency stimulation of the dendritic spine (Chen et al., 1999; Zhu et al., 2015). We compared synaptic weight predictions for a single calcium transient to those due to a pulse train of activation at a single frequency (Fig. S13). However, further investigation should be done to more closely consider the role of stimulus magnitude and frequency on synaptic weight update. In addition, it is important to note that this calcium model and these dendritic spine geometries are representative of hippocampal pyramidal neurons. Calcium signaling, dendritic spine structure, and synaptic weight induction are neuron type specific, and other studies, including some MCell simulations, have investigated calcium signaling and synaptic plasticity in other neuron types (Friedhoff et al., 2021; Antunes and Simoes-de-Souza, 2018; Antunes and Simoes de Souza, 2020; Koumura et al., 2014). In some neuron types, including Purkinje cells, calcium release from the ER can play a vital role in calcium dynamics and subsequent synaptic plasticity (Koumura et al., 2014); thus, care must be taken when considering different neuron types.

In summary, our computational models using idealized and realistic geometries of dendritic spines have identified potential relationships between spine geometry and synaptic weight change that emerge despite the inherent stochasticity of calcium transients. We predict that dendritic spine morphology alters calcium dynamics to achieve their characteristic functions; in particular, so that filopodia can quickly change their synaptic weight, large mushroom spines can solidify their synaptic connections, and intermediate-sized spines require more activation to achieve larger synaptic weight changes. Additionally, we predict that within a certain spine shape, increasing volume (and increasing volume-to-surface-area ratio), while assuming receptors and channels are also recruited, allows for a larger future increase in synaptic weight, suggesting that the volume change associated with LTP and LTD serves to reinforce the biochemical changes during synaptic plasticity. Therefore, spine morphology tunes synaptic response. The advances in computational modeling and techniques have set the stage for a detailed exploration of biophysical processes in dendritic spines (Miermans et al., 2017; Basnayake et al., 2019; Ohadi and Rangamani, 2019). Such efforts are critical for identifying emergent properties of systems behavior and also eliminating hypotheses that are physically infeasible (Bell and Rangamani, 2021; Lee et al., 2021). Models such as this and others can set the stage for investigating longer-time-scale events in spines, including the downstream effectors of calcium (Jędrzejewska-Szmek et al., 2017; Mäki-Marttunen et al., 2020; Hayer and Bhalla, 2005; Ordyan et al., 2020), and actin remodeling for structural plasticity (Bonilla-Quintana et al., 2020; Rangamani et al., 2014).

Acknowledgments

Jeanne M. Nerbonne served as editor.

We thank Dr. Tom Bartol for helpful discussions on the use of MCell and Drs. Lingxia Qiao and Ali Khalilimeybodi for comments and proofreading.

This work was supported by a National Defense Science and Engineering Graduate Fellowship to M.K. Bell, a Hartwell Foundation Postdoctoral Fellowship and Kavli Institute of Brain and Mind Innovative Research Grant #2021-1755 to C.T. Lee, and Air Force Office of Scientific Research FA9550-18-1-0051 to P. Rangamani. MCell development is supported by the National Institute of General Medical Sciences-funded (P41- GM103712) National Center for Multiscale Modeling of Biological Systems (MMBioS).

The authors declare no competing financial interests.

Author contributions: Conceptualization: M.K. Bell, C.T. Lee, P. Rangamani; data curation: M.V. Holst, M.K. Bell, C.T. Lee; formal analysis: M.K. Bell, M.V. Holst; funding acquisition: P. Rangamani; investigation: M.K. Bell, M.V. Holst; methodology: M.K. Bell, C.T. Lee, P. Rangamani; project administration: M.K. Bell, C.T. Lee, P. Rangamani; resources: C.T. Lee, P. Rangamani; software: M.V. Holst; supervision: M.K. Bell, C.T. Lee, P. Rangamani; validation: M.K. Bell, M.V. Holst; visualization: M.K. Bell, M.V. Holst; writing - original draft: M.K. Bell, M.V. Holst, C.T. Lee, P. Rangamani; writing - review & editing: M.K. Bell, M.V. Holst, C.T. Lee, P. Rangamani.

Submitted: 11 June 2021
Revised: 28 May 2022
Accepted: 7 June 2022

References

Alimohamadi, H., M.K. Bell, S. Halpain, and P. Rangamani. 2021. Mechanical principles governing the shapes of dendritic spines. *Front. Physiol.* 12: 657074. https://doi.org/10.3389/fphys.2021.657074

Antunes, G., and M.F. Simoes de Souza. 2020. 3D modeling of dendritic spines with synaptic plasticity. *J. Vis. Exp.* 159:e60896. https://doi.org/10.3791/60896

Antunes, G., and F.M. Simoes-de-Souza. 2018. AMPA receptor trafficking and its role in heterosy naptic plasticity. *Sci. Rep.* 8:1–14. https://doi.org/10.1038/s41598-018-28581-w

Anwar, H., I. Hepburn, H. Nedelescu, W. Chen, and E. De Schutter. 2013. Stochastic calcium mechanisms cause dendritic calcium spike variability. *J. Neurosci.* 33:15848–15867. https://doi.org/10.1523/JNEUROSCI.1722-13.2013

Augustine, G.J., F. Santamaria, and K. Tanaka. 2003. Local calcium signaling in neurons. *Neuron*. 40:331–346. https://doi.org/10.1016/s0896-6273(03)00639-1

Bartol, T.M., D.X. Keller, J.P. Kinney, C.L. Bajaj, K.M. Harris, T.J. Sejnowski, and M.B. Kennedy. 2015. Computational reconstitution of spine calcium transients from individual proteins. *Front. Synaptic Neurosci.* 7:17. https://doi.org/10.3389/fnsyn.2015.00017

Basnayake, K., D. Mazaud, A. Bemelmans, N. Rouach, E. Korkotian, and D. Holcman. 2019. Fast calcium transients in dendritic spines driven by extreme statistics. *PLoS Biol.* 176:e2006202. https://doi.org/10.1371/journal.pbio.2006202

Basnayake, K., D. Mazaud, L. Kushnireva, A. Bemelmans, N. Rouach, E. Korkotian, and D. Holcman. 2021. Nanoscale molecular ar chitecture controls calcium diffusion and ER replenishment in dendritic spines. *Sci. Adv.* 738:eabh1376. https://doi.org/10.1126/sciadv.abh1376

Bell, M.K., and P. Rangamani. 2021. Design decisions for incorporating spatial and mechanical aspects in models of signaling networks. *Curr. Opin. Syst. Biol.* 25:70–77. https://doi.org/10.1016/j.coisb.2021.03.004

Bell, M., T. Bartol, T. Sejnowski, and P. Rangamani. 2019. Dendritic spine geometry and SpApp organization govern the spatiotemporal dynamics of calcium. *J. Gen. Physiol.* 1518:1017–1034. https://doi.org/10.1085/jgp.201812261

Bhalla, U.S. 2004. Signaling in small subcellular volumes. I. Stochastic and diffusion effects on individual pathways. *Biophys. J.* 87:733–744. https://doi.org/10.1529/biophysj.104.040469

Bonilla-Quintana, M., F. Worgotter, C. Tetzlaff, and M. Fauth. 2020. Modeling the shape of synaptic spines by their actin dy namics. *Front. Synaptic Neurosci.* 12:9. https://doi.org/10.3389/fnsyn.2020.00009

Borczyk, M., M.A. Sliwinska, A. Caly, T. Bernas, and K. Radwanska. 2019. Neuronal plasticity affects correlation between the size of den dritic spine and its postsynaptic density. *Sci. Rep.* 9:1693. https://doi.org/10.1038/s41598-018-38412-7

Bourne, J.N., and K.M. Harris. 2008. Balancing structure and function at hippocampal dendritic spines. *Annu. Rev. Neurosci.* 31:47–67. https://doi.org/10.1146/annurev.neuro.31.060407.125646

Calizo, R.C., M.K. Bell, A. Ron, M. Hu, S. Bhattacharya, N.J. Wong, W.G.M. Janssen, G. Perumal, P. Pederson, S. Scarlata, et al. 2020. Cell shape regulates subcellular organelle location to control early Ca^{2+} signal dynamics in vascular smooth muscle cells. *Sci. Rep.* 10:17866. https://doi.org/10.1038/s41598-020-74700-x

Cannon, R.C., C. O'Donnell, and M.F. Nolan. 2010. Stochastic ion channel gating in dendritic neurons: Morphology dependence and probabilistic synaptic activation of dendritic spikes. *PLoS Comput. Biol.* 68:e1000886. https://doi.org/10.1371/journal.pcbi.1000886

Chen, H.X., N. Otmakhov, and J. Lisman. 1999. Requirements for LTP induction by pairing in hippocampal CA1 pyramidal cells. *J. Neurophysiol.* 82:526–532. https://doi.org/10.1152/jn.1999.82.2.526

Chirillo, M.A., M.S. Waters, L.F. Lindsey, J.N. Bourne, and K.M. Harris. 2019. Local resources of polyribosomes and SER promote synapse enlargement and spine clustering after long-term potentiation in adult rat hippocampus. *Sci. Rep.* 91:3861. https://doi.org/10.1038/s41598-019-40520-x

Cho, K., J.P. Aggleton, M.W. Brown, and Z.I. Bashir. 2001. An experimental test of the role of postsynaptic calcium levels in determining synaptic strength using perirhinal cortex of rat. *J. Physiol.* 532:459–466. https://doi.org/10.1111/j.1469-7793.2001.0459f.x

Cormier, R.J., A.C. Greenwood, and J.A. Connor. 2001. Bidirectional synaptic plasticity correlated with the magnitude of dendritic calcium transients above a threshold. *J. Neurophysiol.* 85:399–406. https://doi.org/10.1152/jn.2001.85.1.399

Cornelisse, L.N., R.A.J. van Elburg, R.M. Meredith, R. Yuste, and H.D. Mansvelder. 2007. High speed two-photon imaging of calcium dynamics in dendritic spines: Consequences for spine calcium kinetics and buffer capacity. *PLoS One*. 210:e1073. https://doi.org/10.1371/journal.pone.0001073

Cugno, A., T.M. Bartol, T.J. Sejnowski, R. Iyengar, and P. Rangamani. 2019. Geometric principles of second messenger dynamics in dendritic spines. *Sci. Rep.* 91:11676. https://doi.org/10.1038/s41598-019-48028-0

Dudman, J.T., and M.F. Nolan. 2009. Stochastically gating ion channels enable patterned spike firing through activity-dependent modulation of spike probability. *PLoS Comput. Biol.* 5:e1000290. https://doi.org/10.1371/journal.pcbi.1000290

Earnshaw, B.A., and P.C. Bressloff. 2006. Biophysical model of AMPA receptor trafficking and its regulation during long-term potentiation/long-term depression. *J. Neurosci.* 26:12362–12373. https://doi.org/10.1523/JNEUROSCI.3601-06.2006

Faisal, A.A., J.A. White, and S.B. Laughlin. 2005. Ion-channel noise places limits on the miniaturization of the brain's wiring. *Curr. Biol.*1512:1143–1149. https://doi.org/10.1016/j.cub.2005.05.056

Franks, K.M., T.M. Bartol, and T.J. Sejnowski. 2002. A Monte Carlo model reveals independent signaling at central glutamatergic synapses. *Biophys. J.* 83:2333–2348. https://doi.org/10.1016/S0006-3495(02)75248-X

García-López, P., G.-M. Virginia, and M. Freire. 2010. Dendritic spines and devel opment: Towards a unifying model of spinogenesis—a present day review of Cajal's histological slides and drawings. *Neural Plast.* 769207. https://doi.org/10.1155/2010/769207

Friedhoff, V.N., L. Ramlow. 2021. Models of stochastic Ca^{2+} spiking. *Eur. Phys. J. Spec. Top.* 23014:2911–2928. https://doi.org/10.1140/epjs/s11734-021-00174-1

Friedhoff, V.N., G. Antunes, M. Falcke, and F.M. Simoes de Souza. 2021. Stochastic reaction-diffusion modeling of calcium dynamics in 3D-dendritic spines of Purkinje cells. *Biophys. J.* 120:2112–2123. https://doi.org/10.1016/j.bpj.2021.03.027

Fujii, M., K. Ohashi, Y. Karasawa, M. Hikichi, and S. Kuroda. 2017. Small-volume effect enables robust, sensitive, and efficient information transfer in the spine. *Biophys. J.* 112:813–826. https://doi.org/10.1016/j.bpj.2016.12.043

Graupner, M., and N. Brunel. 2012. Calcium-based plasticity model explains sensitiv ity of synaptic changes to spike pattern, rate, and dendritic location. *Proc. Natl. Acad. Sci. U S A.* 10910:3991–3996. https://doi.org/10.1073/pnas.1109359109

Griffith, T., K. Tsaneva-Atanasova, and J.R. Mellor. 2016. Control of Ca^{2+} influx and calmodulin activation by SK-channels in dendritic spines. *PLoS Comput. Biol.* 125:e1004949. https://doi.org/10.1371/journal.pcbi.1004949

Harris, K.M., F. Jensen, F.E. Jensen, B. Tsao, and B. Tsao. 1992. Three-dimensional structure of dendritic spines and synapses in rat hippocampus (CA1) at postnatal day 15 and adult ages: Implications for the maturation of synaptic physiology and long-term potentiation. *J. Neurosci.* 127:2685–2705. https://doi.org/10.1523/jneurosci.12-07-02685.1992

Hayer, A., and U.S. Bhalla. 2005. Molecular switches at the synapse emerge from re ceptor and kinase traffic. *PLoS Comput. Biol.* 12:e20. https://doi.org/10.1371/journal.pcbi.0010020

Héja, L., Z. Szabo, M. Peter, and J. Kardos. 2021. Spontaneous Ca^{2+} fluctuations arise in thin astrocytic processes with real 3D geometry. *Front. Cell. Neurosci.* 15:617989. https://doi.org/10.3389/fncel.2021.617989

Holcman, D., Z. Schuss, and E. Korkotian. 2004. Calcium dynamics in dendritic spines and spine motility. *Biophys. J.* 87:81–91. https://doi.org/10.1529/biophysj.103.035972

Holcman, D., E. Korkotian, and M. Segal. 2005. Calcium dynamics in dendritic spines, modeling and experiments. *Cell Calcium*. 375:467–475. https://doi.org/10.1016/j.ceca.2005.01.015

Holthoff, K., D. Tsay, and R. Yuste. 2002. Calcium dynamics of spines depend on their dendritic location. *Neuron*. 333:425–437. https://doi.org/10.1016/s0896-6273(02)00576-7

Hoogland, T.M., and P. Saggau. 2004. Facilitation of L-type Ca^{2+} channels in dendritic spines by activation of β2 adrenergic receptors. *J. Neurosci.* 24:8416–8427. https://doi.org/10.1523/JNEUROSCI.1677-04.2004

Hu, E., A. Mergenthal, C.S. Bingham, D. Song, J.M. Bouteiller, and T.W. Berger. 2018. A glutamatergic spine model to enable multi-scale modeling of nonlinear calcium dynamics. *Front. Comput. Neurosci.* 12:58. https://doi.org/10.3389/fncom.2018.00058

Jahr, Craig E., and Charles F. Stevens. 1993. Calcium permeability of the *N*-methyl-D-aspartate receptor channel in hippocampal neurons in culture. *Proc. Natl. Acad. Sci. USA*. 9024:11573–11577. https://doi.org/10.1073/pnas.90.24.11573

Jasinska, M., E. Jasek-Gajda, O. Woznicka, G.J. Lis, E. Pyza, and J.A. Litwin. 2019. Circadian clock regulates the shape and content of dendritic spines in mouse barrel cortex. *PLoS One*. 1411:e0225394. https://doi.org/10.1371/journal.pone.0225394

Jędrzejewska-Szmek, J., S. Damodaran, D.B. Dorman, and K.T. Blackwell. 2017. Calcium dynamics predict direction of synaptic plas ticity in

striatal spiny projection neurons. *Eur. J. Neurosci.* 45:1044–1056. https://doi.org/10.1111/ejn.13287

Jonas, P., G. Major, and B. Sakmann. 1993. Quantal components of unitary EPSCs at the mossy fibre synapse on CA3 pyramidal cells of rat hippocampus. *J. Physiol.* 472:615–663. https://doi.org/10.1113/jphysiol.1993.sp019965

Kanjhan, R., P.G. Noakes, and M.C. Bellingham. 2016. Emerging roles of filopodia and dendritic spines in motoneuron plasticity during development and disease. *Neural Plast.* 3423267. https://doi.org/10.1155/2016/3423267

Kasai, H., M. Matsuzaki, J. Noguchi, N. Yasumatsu, and H. Nakahara. 2003. Structure–stability–function relationships of dendritic spines. *Trends Neurosci.* 26:360–368. https://doi.org/10.1016/S0166-2236(03)00162-0

Keller, D.X., K.M. Franks, T.M. Bartol Jr, and T.J. Sejnowski. 2008. Calmodulin activation by calcium transients in the postsynaptic den sity of dendritic spines. *PLoS One.* 34:e2045. https://doi.org/10.1371/journal.pone.0002045

Kerr, R.A., T.M. Bartol, B. Kaminsky, M. Dittrich, J.C.J. Chang, S.B. Baden, T.J. Sejnowski, and J.R. Stiles. 2008. Fast Monte Carlo simulation methods for biological reaction-diffusion systems in solution and on surfaces. *SIAM J. Sci. Comput.*30:3126. https://doi.org/10.1137/070692017

Kotaleski, J.H., and K.T. Blackwell. 2010. Modelling the molecular mechanisms of synaptic plasticity using systems biology approaches. *Nat. Rev. Neurosci.* 11:239–251. https://doi.org/10.1038/nrn2807

Koumura, T., H. Urakubo, K. Ohashi, M. Fujii, and S. Kuroda. 2014. Stochasticity in Ca^{2+} increase in spines enables robust and sen sitive information coding. *PLoS One.* 96:e99040. https://doi.org/10.1371/journal.pone.0099040

Kummer, U., B. Krajnc, J. Pahle, A.K. Green, C.J. Dixon, and M. Marhl. 2005. Transition from stochastic to deterministic behavior in calcium os cillations. *Biophys. J.* 89:1603–1611. https://doi.org/10.1529/biophysj.104.057216

Lee, C.T., J.G. Laughlin. 2020. 3D mesh processing using GAMer 2 to enable reaction-diffusion simulations in realistic cellular geometries. *PLoS Comp. Bio.* 16:e1007756.

Lee, K.F.H., C. Soares, and J.-C. Béïque. 2012. Examining form and function of dendritic spines. *Neural Plast.* 2012. 704103. https://doi.org/10.1155/2012/704103

Lee, C.T., J.G. Laughlin, J.B. Moody, R.E. Amaro, J.A. McCammon, M. Holst, and P. Rangamani. 2020. An open-source mesh generation platform for biophys ical modeling using realistic cellular geometries. *Biophys. J.* 118:1003–1008. https://doi.org/10.1016/j.bpj.2019.11.3400

Lee, C.T., M. Akamatsu, and P. Rangamani. 2021. Value of models for membrane budding. *Curr. Opin. Cell Biol.* 71:38–45. https://doi.org/10.1016/j.ceb.2021.01.011

Lisman, J. 2017. Glutamatergic synapses are structurally and biochemically complex be cause of multiple plasticity processes: Long-term potentiation, long-term depression, short-term potentiation and scaling. *Philos. Trans. R. Soc. Lond. B Biol. Sci.* 3721715:20160260. https://doi.org/10.1098/rstb.2016.0260

Lohmann, C., and T. Bonhoeffer. 2008. A role for local calcium signaling in rapid synaptic partner selection by dendritic filopodia. *Neuron.* 59:253–260. https://doi.org/10.1016/j.neuron.2008.05.025

Mahajan, G., and S. Nadkarni. 2019. Intracellular calcium stores mediate metaplasticity at hippocampal dendritic spines. *J. Physiol.* 597:3473–3502. https://doi.org/10.1113/JP277726

Mäki-Marttunen, T., N. Iannella, A.G. Edwards, G.T. Einevoll, and K.T. Blackwell. 2020. A unified computational model for cortical postsynaptic plasticity. *Elife.* 9:e55714. https://doi.org/10.7554/eLife.55714

Matsuzaki, M. 2007. Factors critical for the plasticity of dendritic spines and memory stor age. *Neurosci. Res.* 57:1–9. https://doi.org/10.1016/j.neures.2006.09.017

Miermans, C.A., R.P.T. Kusters, C.C. Hoogenraad, and C. Storm. 2017. Biophysical model of the role of actin remodeling on dendritic spine morphology. *PLoS One.* 122:e0170113. https://doi.org/10.1371/journal.pone.0170113

Murakoshi, H., and R. Yasuda. 2012. Postsynaptic signaling during plasticity of dendritic spines. *Trends Neurosci.* 35:135–143. https://doi.org/10.1016/j.tins.2011.12.002

Naraghi, M., and E. Neher. 1997. Linearized buffered Ca^{2+} diffusion in microdomains and its implications for calculation of (Ca^{2+}) at the mouth of a calcium channel. *J. Neurosci.* 17:6961–6973. https://doi.org/10.1523/jneurosci.17-18-06961.1997

Neves, S.R., P. Tsokas, A. Sarkar, E.A. Grace, P. Rangamani, S.M. Taubenfeld, C.M. Alberini, J.C. Schaff, R.D. Blitzer, I.I. Moraru, and R. Iyengar. 2008. Cell shape and negative links in regulatory motifs together control spatial information flow in signaling networks. *Cell.* 1334:666–680. https://doi.org/10.1016/j.cell.2008.04.025

Nishiyama, J., and R. Yasuda. 2015. Biochemical computation for spine structural plastic ity. *Neuron.* 871:63–75. https://doi.org/10.1016/j.neuron.2015.05.043

Ofer, N., D.R. Berger, N. Kasthuri, J.W. Lichtman, and R. Yuste. 2021. Ultrastructural analysis of dendritic spine necks reveals a continuum of spine morphologies. *Developmental Neurobiology*. https://doi.org/10.1002/dneu.22829

Ohadi, D., and P. Rangamani. 2019. Geometric control of frequency modulation of cAMP oscillations due to calcium in dendritic spines. *Biophys. J.* 117:1981. https://doi.org/10.1016/j.bpj.2019.10.004

Ohadi, D., D.L. Schmitt, B. Calabrese, S. Halpain, J. Zhang, and P. Rangamani. 2019. Computational modeling reveals frequency modu lation of calcium-cAMP/PKA pathway in dendritic spines. *Biophys. J.* 117:1963–1980. https://doi.org/10.1016/j.bpj.2019.10.003

Ordyan, M., T. Bartol, M. Kennedy, P. Rangamani, and T. Sejnowski. 2020. Interactions between calmodulin and neurogranin govern the dy namics of CaMKII as a leaky integrator. *PLoS Comput. Biol.* 167:e1008015. https://doi.org/10.1371/journal.pcbi.1008015

Ozcan, A.S. 2017. Filopodia: A rapid structural plasticity substrate for fast learning. *Front. Synaptic Neurosci.* 9:12. https://doi.org/10.3389/fnsyn.2017.00012

O'Donnell, C. and M.F. Nolan. 2014. Stochastic ion channel gating and probabilistic computation in dendritic neurons. *In* The Computing Dendrite. H. Cuntz, M.W.H. Remme, B. Torben-Nielsen, editors. Springer. New York. 397–414.

O'Donnell, C., M.F. Nolan, and M.C.W. van Rossum. 2011. Dendritic spine dynam ics regulate the long-term stability of synaptic plasticity. *J. Neurosci.* 31:16142–16156. https://doi.org/10.1523/jneurosci.2520-11.2011

Perez-Alvarez, A., F. Huhn, C.D. Dürst, A. Franzelin, P.J. Lamothe-Molina, T.G. Oertner. 2020. Endoplasmic reticulum visits highly active spines and pre vents runaway potentiation of synapses. *Nat. Commun.* 11:1–10. https://doi.org/10.1038/s41467-020-18889-5

Rangamani, P., A. Lipshtat, E.U. Azeloglu, R.C. Calizo, M. Hu, S. Ghassemi, J. Hone, S. Scarlata, S.R. Neves, and R. Iyengar. 2013. Decoding information in cell shape. *Cell.* 1546:1356–1369. https://doi.org/10.1016/j.cell.2013.08.026

Rangamani, P., G.Y. Xiong, and R. Iyengar. 2014. Multiscale modeling of cell shape from the actin cytoskeleton. *Prog. Mol. Biol. Transl. Sci.* 123:143–167. https://doi.org/10.1016/B978-0-12-397897-4.00002-4

Robinson, R.A., and R.H. Stokes. 1959. Electrolyte Solutions. Butterworths Scientific Publications, .

Rodrigues, Y.E., C. Tigaret, H. Marie, C. O'Donnell, and R. Veltz. 2022. A stochastic model of hippocampal synaptic plasticity with geometrical readout of enzyme dynamics. *bioRxiv*. https://doi.org/10.1101/2021.03.30.437703

Rodriguez, A., D.B. Ehlenberger, D.L. Dickstein, P.R. Hof, and S.L. Wearne. 2008. Automated three-dimensional detection and shape classification of dendritic spines from fluorescence microscopy images. *PLoS One.* 34:e1997. https://doi.org/10.1371/journal.pone.0001997

Rubin, J.E., R.C. Gerkin, G.Q. Bi, and C.C. Chow. 2005. Calcium time course as a signal for spike-timing–dependent plasticity. *J. Neurophysiol.* 93:2600–2613. https://doi.org/10.1152/jn.00803.2004

Rüdiger, S. 2014. Stochastic models of intracellular calcium signals. *Phys. Rep.* 534:39–87.

Ruhl, D.A., E. Bomba-Warczak, E.T. Watson, M.M. Bradberry, T.A. Peterson, T. Basu, A. Frelka, C.S. Evans, J.S. Briguglio, T. Basta, et al. 2019. Synaptotagmin 17 controls neurite outgrowth and synaptic physiology via distinct cellular pathways. *Nat. Commun.* 10:3532. https://doi.org/10.1038/s41467-019-11459-4

Sabatini, B.L., and K. Svoboda. 2000. Analysis of calcium channels in single spines using optical fluctuation analysis. *Nature.* 4086812:589–593. https://doi.org/10.1038/35046076

Sabatini, B.L., T.G. Oertner, and K. Svoboda. 2002. The life cycle of Ca^{2+} ions in dendritic spines. *Neuron.* 333:439–452. https://doi.org/10.1016/s0896-6273(02)00573-1

Schmidt, H. 2012. Three functional facets of calbindin D-28k. *Front. Mol. Neurosci.* 5:25. https://doi.org/10.3389/fnmol.2012.00025

Schmidt, H., and J. Eilers. 2009. Spine neck geometry determines spino-dendritic cross talk in the presence of mobile endogenous calcium binding proteins. *J. Comput. Neurosci.* 27:229–243. https://doi.org/10.1007/s10827-009-0139-5

Schoberl, J. 1997. NETGEN an advancing front 2D/3D-mesh generator based on abstract rules. *Comput. Vis. Sci.* 1:41–52. https://doi.org/10.1007/s007910050004

Schwaller, B. 2010. Cytosolic Ca^{2+} buffers. *Cold Spring Harbor Perspect. Biol.* 2: a004051. https://doi.org/10.1101/cshperspect.a004051

Scott, K.E., S.I. Fraley, and P. Rangamani. 2021. A spatial model of YAP/TAZ signaling reveals how stiffness, dimensionality, and shape contribute to emergent outcomes. *Proc. Natl. Acad. Sci. USA.* 118:e2021571118. https://doi.org/10.1073/pnas.2021571118

Segal, M. 2010. Dendritic spines, synaptic plasticity and neuronal survival: Activity shapes dendritic spines to enhance neuronal viability. *Eur. J. Neurosci.* 31:2178–2184. https://doi.org/10.1111/j.1460-9568.2010.07270.x

Segal, M., and E. Korkotian. 2014. Endoplasmic reticulum calcium stores in dendritic spines. *Front. Neuroanat.* 8:64. https://doi.org/10.3389/fnana.2014.00064

Shouval, H.Z., M.F. Bear, and L.N. Cooper. 2002. A unified model of NMDA receptor dependent bidirectional synaptic plasticity. *Proc. Natl. Acad. Sci. USA.* 99:10831–10836. https://doi.org/10.1073/pnas.152343099

Skupin, A., H. Kettenmann, and M. Falcke. 2010. Calcium signals driven by single channel noise. *PLoS Comput. Biol.* 68:e1000870. https://doi.org/10.1371/journal.pcbi.1000870

Sorra K.E. and Harris K.M. 2000. Overview on the structure, composition, function, development, and plasticity of hippocampal dendritic spines. *Hippocampus*. 10:501–511. https://doi.org/10.1002/1098-1063(2000)10:5<501::AID-HIPO1>3.0.CO;2-T

Spacek, J., and K.M. Harris. 1997. Three-dimensional organization of smooth endoplas mic reticulum in hippocampal CA1 dendrites and dendritic spines of the immature and mature rat. *J. Neurosci.* 17:190–203. https://doi.org/10.1523/jneurosci.17-01-00190.1997

Stein, I.S., and K. Zito. 2019. Dendritic spine elimination: Molecular mechanisms and implications. *Neuroscientist*. 251:27–47. https://doi.org/10.1177/1073858418769644

Stiles, J.R., and T.M. Bartol. 2001. Monte Carlo methods for simulating realistic synaptic microphysiology using MCell. *Comput. Neurosci.*87–127.

Stiles, J.R., D. Van Helden, T.M. Bartol Jr., E.E. Salpeter, and M.M. Salpeter. 1996. Miniature endplate current rise times <100 μ s from improved dual recordings can be modeled with passive acetylcholine diffusion from a synaptic vesicle. *Proc. Natl. Acad. Sci. USA.* 93:5747–5752. https://doi.org/10.1073/pnas.93.12.5747

Tottori, T., M. Fujii, and S. Kuroda. 2019. NMDAR-mediated Ca^{2+} increase shows robust information transfer in dendritic spines. *Biophys. J.* 116: 1748–1758. https://doi.org/10.1016/j.bpj.2019.03.030

Vargas-Caballero, M., and H.P. Robinson. 2004. Fast and slow voltage-dependend dynamics of magnesium block in the NMDA receptor: The asymmetric trapping block model. *J. Neurosci.* 24:6171–6180. https://doi.org/10.1523/jneurosci.1380-04.2004

Volfovsky, N., H.Parnas, M.Segal, and E.Korkotian. 1999. Geometry of dendritic spines affects calcium dynamics in hip pocampal neurons: Theory and experiments. *J. Neurophysiol.* 82:450–462. https://doi.org/10.1152/jn.1999.82.1.450

Wasserstein, R.L., L. AllenSchirm, and N.A. Lazar. 2019. Moving to a world beyond "p < 0.05". *Am. Statistician*. 73:1–19. https://doi.org/10.1080/000031305.2019.1583913

Wu, Y., C. Whiteus, C.S. Xu, K.J. Hayworth, R.J. Weinberg, H.F. Hess, and P. De Camilli. 2017. Contacts between the endoplasmic reticulum and other membranes in neurons. *Proc. Natl. Acad. Sci. USA.* 11424: E4859–E4867. https://doi.org/10.1073/pnas.1701078114

Xia, Z., and D.R. Storm. 2005. The role of calmodulin as a signal integrator for synaptic plasticity. *Nat. Rev. Neurosci.* 6:267–276. https://doi.org/10.1038/nrn1647

Yasuda, R. 2017. Biophysics of biochemical signaling in dendritic spines: Implications in synaptic plasticity. *Biophys. J.* 113:2152–2159. https://doi.org/10.1016/j.bpj.2017.07.029

Yasuda, R., E.A. Nimchinsky, V. Scheuss, T.A. Pologruto, T.G. Oertner, B.L. Sabatini, and K. Svoboda. 2004. Imaging calcium concentration dynamics in small neuronal com partments. *Sci. STKE.* 2004:pl5. https://doi.org/10.1126/stke.2192004pl5

Yuste, R. 2010. Dendritic Spines. MIT Press. Cambridge.

Yuste, R., and T. Bonhoeffer. 2004. Genesis of dendritic spines: Insights from ultrastruc tural and imaging studies. *Nat. Rev. Neurosci.* 51:24–34. https://doi.org/10.1038/nrn1300

Yuste, R., W. Denk, and W. Denk. 1995. Dendritic spines as basic functional units of neuronal integration. *Nature*. 3756533:682–684. https://doi.org/10.1038/375682a0

Yuste, R., A. Majewska, and K. Holthoff. 2000. From form to function: Calcium compart mentalization in dendritic spines. *Nat. Neurosci.* 37:653. https://doi.org/10.1038/76609

Zhu, G., Y. Liu, Y. Wang, X. Bi, and M. Baudry. 2015. Different patterns of electrical activity lead to long-term potentiation by activating different intracellular pathways. *J. Neurosci.* 35:621–633. https://doi.org/10.1523/JNEUROSCI.2193-14.2015

Supplemental material

We constructed a stochastic model of calcium influx into dendritic spines of different morphologies. In this model are calcium influx through various receptors and channels and calcium efflux through various pumps localized to the PM or SpApp (a specialized form of ER). Each simulation condition was run with 50 random seeds. We then took the stochastic calcium temporal dynamics and input them into deterministic equations for synaptic weight update. Using this framework, we can vary spine size and shape to see how geometric factors influence weight updates. We specifically considered calcium dynamics in terms of total calcium ions.

Model readouts

We simulated synaptic weight updates for each of the 50 calcium transients and then took the mean and SD of the synaptic weight prediction. Because we are working with a stochastic model and are considering Ca^{2+} in terms of ions, we converted the parameters in the synaptic weight equations from units involving concentration to units of molecules, based on average spine volumes and realistic numbers of calcium ions in dendritic spines. It is important to note that using total Ca^{2+} ions is a global view of the dendritic spine, while concentration can be considered as more of a local measurement. As mentioned, this synaptic weight change is a phenomenological relationship between Ca^{2+} and synaptic weight that captures the concept of synaptic strength change, and it remains unclear if using ions versus concentration is a better approach for predicting this change.

We converted our results into average concentrations by dividing the calcium transients by the respective spine volume, converting our synaptic weight parameters into units of concentration, and rerunning our synaptic weight calculations (Fig. S10). Interestingly, we see a different trend within the concentration simulations versus total ion simulations. We believe the relationship between spine volume and calcium influx is leading to these differences and requires further investigation (O'Donnell et al., 2011). We believe that the synaptic weight model might also be parameter dependent, in particular with regard to β_P, β_D, θ_P, and θ_D. This again brings into question the approach of local versus global calcium readouts and how to capture these effects with the parameters in phenomenological models. Further investigation is required to understand the considerations behind these different approaches.

Multiple pulses of calcium

We consider the case in which a spine is activated multiple times to produce a series of calcium pulses and predict the synaptic weight update from this series of calcium pulses. To do this, we repeated each calcium pulse 10 times with 35 ms between activation events. We note that this is an assumption that has potential consequences on our results. However, for simplicity, we assume the same calcium transient for each pulse train. We input these calcium pulse trains into the synaptic weight equations.

Matlab analysis of Ca^{2+} transients

We used Matlab v2018b to analyze the max Ca^{2+} peak and decay time constants for the stochastic Ca^{2+} results. For each realization of the Ca^{2+} transient, we used the max() function to find the peak Ca^{2+} value and corresponding time. We fitted the transient after the peak using the fit() function set to exp1. The parameters from each fit, corresponding to a realization from a random seed, and statistics such as the mean and SD were computed. The SEM was found by dividing the SD by the square root of the number of individual trials, in this case 50 trials.

Statistical analysis

Statistical significance was determined using two-tailed two-sample *t* test assuming equal means and variance (ttest2() function) in Matlab v2018b with a significance cutoff at $P = 0.05$. Statistical comparisons were made between the distributions of observables yielded by the 50 simulations of the compared experimental conditions. Trends in the stochastic results data were fitted using all 50 seeds for each of the simulations being considered in the fit. The reported trend lines were estimated using the data from all 50 seeds, as opposed to fitting to the means only. Linear fits and exponential fits were computed in Matlab using the functions fitlim() and fit(), respectively. We highlight that we are using the classic approach of null-hypothesis significance testing, P values, and statistically significant verbiage, which has been questioned as perilous and oversimplistic (Wasserstein et al., 2019). We have provided the P values for each result comparison for closer consideration (Fig. S12). The linear and exponential trend lines shown have a range of r^2 values and are used to show general trends. We emphasize, however, that in some plots we fitted to either very few data points or a small domain. Therefore, we reiterate that these factors limit the interpretation of the quantitative nature of the fits.

Geometries

Idealized, axisymmetric geometries were used to represent the structure of dendritic spines in this study. Three general spine shapes are represented—thin, mushroom-shaped, and filopodia-shaped—and each shape is further varied in size and, for the thin and mushroom spines, neck radius.

Geometry generation

The geometries were generated from 2-D ideal spine profiles obtained from Alimohamadi et al. (2020) consisting of a series of points (r, z) that form the outline of the respective geometry's rotational cross section. Using Netgen/NGSolve v6.2 (Schoberl, 1997), we revolved these profiles about the z-axis to yield a rotationally symmetric 3-D spine geometry (Fig. S1). In all spine geometries, a circular PSD was centered at the top of the spine head. The PSD area was set as a function of spine volume according to the relationship observed in Borczyk et al. (2019).

Size and neck variations

To further explore the effects of geometric variations on calcium transients and stochasticity, and to facilitate the comparison of spine geometries of similar volumes and different shapes, the base geometries of all three shapes were scaled to two additional volumes beyond the base shapes from Alimohamadi et al. (2021). The additional versions of the thin spine, initially smaller than the other spine shapes, were scaled such that their length measurements were 1.5 and 2 times their original values, resulting in volumes 3.375 and 8 times that of the initial thin spine, respectively. The base mushroom spine, intermediate in volume, was scaled to 0.66 and 1.33 times its original size, resulting in volumes 0.287 and 2.353 times its original value, and the base filopodia-shaped spine, initially the largest in volume, was scaled to 0.5 and 0.75 times its original size, resulting in volumes 0.125 and 0.422 times its original volume. This scheme ultimately resulted in three different sizes for each spine shape, spanning a similar range of volumes.

The neck radius of the thin and mushroom spines was also varied, with neck length modified as well to preserve spine volume. To create the different spine sizes, the 2-D spine profiles were dilated about the origin by a certain scale factor, and the resultant image was rotated about its vertical axis using Netgen/NGSolve to produce a scaled-up or scaled-down 3-D geometry. In the thin and mushroom 2-D profiles, the x values of points along the spine neck were scaled by a certain coefficient, and the length of the neck was then scaled by the squared inverse of the coefficient to maintain an approximately constant volume. A list of all spine geometries used, and their respective geometric measures, is in Table S1.

SpApp

Some dendritic spines are observed to have a SpApp, an extension of the smooth ER, extending from the dendrite into the neck and head of the spine (Spacek and Harris, 1997). In this study, the effects of the presence of the SpApp on calcium transients and stochasticity were investigated; to achieve this, the thin and mushroom spine geometries were further modified with the addition of a SpApp of varying sizes. For both spine shapes, the control-sized SpApp geometry was constructed by scaling down the original spine geometry and extending the SpApp neck, such that the SpApp occupied ∼10% of the spine volume and extended to the base of the spine. SpApp size was then varied by scaling the SpApp geometry up and down and changing the neck length such that the SpApp base coincided with the spine base. SpApp was not added to the filopodia-shaped geometry, as the SpApp was not generally found to be present in such spine shapes (Spacek and Harris, 1997). The SpApp-containing geometries are also listed in Table S2.

Realistic geometries

Realistic geometries were chosen from among those on the full dendrite geometry generated in Lee et al. (2020). Briefly, the geometric meshes were generated from electron micrographs in Wu et al. (2017) using GAMer 2 (Lee et al., 2020). Individual spines with labeled PSD and volumes similar to the idealized geometries were selected from the realistic dendritic branch.

Additional simulation results

Artificial calcium transients highlight how calcium peak and pulse duration influence synaptic weight prediction

To graphically solidify the relationship between the calcium and the various synaptic weight update terms, we used artificial calcium transients as input into the synaptic weight model (Fig. S2 a). We considered three different cases: (1) a high calcium level (1,000 ions) for 5 ms, (2) a lower calcium level (300 ions) for 5 ms, and (3) a high calcium level (1,000 ions) for 10 ms. We can clearly see that for the prescribed calcium inputs, the τ_w learning rate filters for rate of change to synaptic weight during the calcium pulse, while Ω_w determines if the synaptic weight increases or decreases (Fig. S2, b and c). We see that as the calcium transient moves within the prescribed thresholds of LTP and LTD, the learning rate increases and decreases, while the Ω_w term flips between negative, positive, and no change. For the selected LTP and LTD thresholds, both high calcium level cases lead to synaptic strengthening, while the lower calcium level case leads to synaptic weakening (Fig. S2 d).

Simulation results versus other geometric parameters show various trends

We plotted maximum Ca^{2+} peak, decay time constant, and synaptic weight against volume for all size variations of filopodia-shaped spines, thin spines, mushroom spines, and mushroom spines with SpApp (Fig. S3). We found similar trends across volume as we observed across volume-to-surface-area ratio. To understand the effect of volume on these calcium readouts, we plotted several calcium transients for different geometries in terms of concentration, by dividing by the respective geometries' volumes (Fig. S4).

Spine neck size shows differences in the large mushroom spines but not the smaller thin spines

The spine neck has long been discussed as a key parameter governing calcium signaling within dendritic spines (Volfovsky et al., 1999). We also explored the effects of varying spine length and radius, while preserving spine volume. We first varied the spine neck on thin spines of the control volume (Fig. S5 a). We saw that while the calcium transients have considerable overlap, the thin-necked spine shows significant variance at later time points compared with the other spines (Fig. S5, b and c). We found no statistically significant differences between peak calcium values and only decay differences between the thinnest and thickest necks (Fig. S5, d and e). Synaptic weight changes for the thin spines with different neck geometries showed no significant differences but were trended toward negative weight changes for thicker necks (Fig. S5 f). We next explored mushroom spines with thinner or thicker neck geometries but with the same volume as the mushroom control spine (Fig. S6 a). While the mean of the calcium transients appeared quite close, there was significant difference in variance for the mushroom spine with the thick neck (Fig. S6, b and c). We saw differences in peak calcium only between the thinnest and thickest of the mushroom neck cases, and no significant difference in decay time constant (Fig. S6, d and e). Synaptic weight calculations show that the presence of the thinnest versus thickest neck on a mushroom spine does lead to statistically significant differences in synaptic weight updates (Fig. S6 f). This indicates that spine neck morphology might have more implications for these larger mushroom spines, compared with the smaller thin spines.

The presence of SpApp in thin spines causes no clear trend in synaptic weight update

We varied the size of SpApp in thin control spines with the SpApp acting as a calcium sink with SERCA pumps (Fig. S7 a). We found that the presence of SpApp makes the calcium transient response more complex, with a double peak visible in the variance for thin spines (Fig. S7, b and c). While we can fit the peak calcium values and decay time constant trends against both volume (Fig. S7, d and e) and volume-to-surface-area ratio (Fig. S7, g and h), SpApp presence shows no clear trend in synaptic weight change for thin spines, and the differences were not statistically significant (Fig. S7 f).

Comparison to previous experimental and computational results

We compared our calcium transients to previously reported experimental and computational studies (Fig. S8). For a more direct comparison, we normalized the various readouts to 1 and time shifted the traces to all begin around the same time point. We considered the mean transient of a small idealized thin spine (0.035 μm^3) and large idealized mushroom spine (0.643 μm^3) from our study. We found that the small thin spine decays quite quickly while the larger mushroom spine has decay dynamics more similar to previously published findings.

Our previous deterministic results match the qualitative trends seen in these results

We previously published a deterministic reaction diffusion model of calcium dynamics in dendritic spines of different morphologies (Bell et al., 2019). We found trends in the peak calcium concentration over spine volumes in that work and wanted to directly compare those results to our findings in this work. Using the results from Bell et al. (2019), we integrated calcium concentration over the spine volume at each time point, found the peak calcium in ions, and fitted the decay dynamics of the calcium transient with an exponential decay function, $c\exp(-kt)$. We compared the peaks and decay time constants over both volume and volume-to-surface-area ratio and found the same qualitative trends as our findings in the current work (Fig. S9). We converted our current findings into concentration by dividing the total calcium ion transients by the geometry volumes and considered five example transients for the three control idealized geometries and three realistic geometries (Fig. S4). We found that the thin spines have the highest concentrations, followed by filopodia, and then mushroom spines.

Synaptic weight changes depend on calculations with ions versus concentration

Synaptic weight update equations are typically phenomenological relationships based on Ca^{2+}. Historically, many mathematical models considering synaptic weight changes have considered synaptic weight changes in terms of concentration (Shouval et al., 2002; O'Donnell et al., 2011; Mahajan and Nadkarni, 2019). In this model, we considered Ca^{2+} in terms of Ca^{2+} ions. We wanted to consider if the use of ions versus concentration influences the synaptic weight update results. We converted the synaptic weight equations by converting the parameters from units involving molecules to concentration by dividing by the average spine volume (0.06 μm^3) and converting to μM. We converted all the Ca^{2+} transients to μM by dividing by each respective spine geometry volume and modifying units. We plotted the synaptic weight change at 35 ms for all simulations when considering ions versus concentration (Fig. S10). We found that synaptic weight change predictions do change when using ions versus concentration, because the concentration also considers the volume of the spines. Using concentration leads to a decreasing trend in synaptic weight with increasing volume, which is the opposite of the trend seen using ions. We did, however, still find protrusion-type specific trends within the overall dynamics.

There are several considerations to make during this comparison. First, as mentioned, the synaptic weight equations used are phenomenological relationships between Ca^{2+} and the concept of synaptic weight, which captures the idea of synaptic strengthening, which would actually occur through the insertion of receptors, such as AMPAR, and potentially spine volume increase. It remains unclear if total ion count, which is a global consideration of the whole spine, or Ca^{2+} concentration, which considers the local

environment, is the correct value to consider for synaptic weight calculations. Furthermore, we used average concentration in Fig. S10, c and d, but dendritic spines are known to have signaling nanodomains, so it could be possible that it would be more accurate to consider peak concentration instead of average concentration for this calculation. Additionally, it is possible that the thresholds for LTP versus LTD need to be modified when considering a global reading, such as total ions in the spine, versus a local measurement, such as local concentration. Should synaptic weight change depend on the total amount of Ca^{2+} influx or the local environment within the spine? This is an ongoing consideration that needs further analysis and discussion.

Another consideration with this analysis is that the synaptic weight update is calcium dependent. We plotted the dynamics of the filopodia-shaped spine for a more direct comparison between calcium transients in terms of calcium ion and concentration (Fig. S11). We can see that even through there is more calcium ion influx as the spines get larger, that increase in influx is not proportional to the increase in spine volume. Said another way, calcium influx is sublinear with respect to volume increase, so larger spines have lower calcium transients. This is a consequence of our assumption of constant receptor density. This idea has been explored quite elegantly in O'Donnell et al. (2011). Therefore, calcium influx related to spine volume should continue to be explored, and the consequences of geometry-dependent calcium trends on phenomenological relationships for synaptic weight need to be investigated further.

Two-tailed t test results for all stochastic simulations

We conducted two-tailed *t* test calculations between all stochastic simulations for both idealized and real geometries for maximum Ca^{2+} peak, decay time constant, and synaptic weight change. We display both the *h* and P values for each comparison (Fig. S12). We use a P threshold of 0.05 to determine the binary *h* value. A P value <0.05 indicates that the two results are statistically different and produces an *h* value of 1; a P value >0.05 indicates that the two results are not statistically different and produces an *h* value of 0. P values have been truncated at two decimal points.

Synaptic weight predictions from a single calcium transient mimic those from a pulse train

For all simulations so far, synaptic weight prediction used a single calcium transient as input. However, usually a dendritic spine receives a pulse train of activation, so we want to consider the consequences of a pulse train of calcium transients on synaptic weight updates. To do this, for each 50 calcium transients per geometry, we repeated the calcium temporal dynamics 10 times with 35 ms between the initiation of the calcium spikes. This induction protocol of 29 Hz is within the regime expected to begin to produce LTP in dendritic spines (Chen et al., 1999; Zhu et al., 2015). We compared the synaptic weight update for a single pulse to the update for a pulse train (Fig. S13, a and b). We found that the synaptic weight change increases in magnitude for the pulse train condition but keeps the same general trends observed in the single-pulse simulations, indicating that a single pulse does give a good approximation of pulse train dynamics at this frequency. However, it is clear that the conversion between single pulse and pulse train is not as clear for the realistic geometry cases. Additionally, the pulse train predictions showed an increase in SD, with more cases showing the ability to increase or decrease their synaptic weight. Therefore, while the mean synaptic weight change for each condition held across a single pulse and multiple pulses, the pulse train widens the synaptic weight regime that a spine can enter.

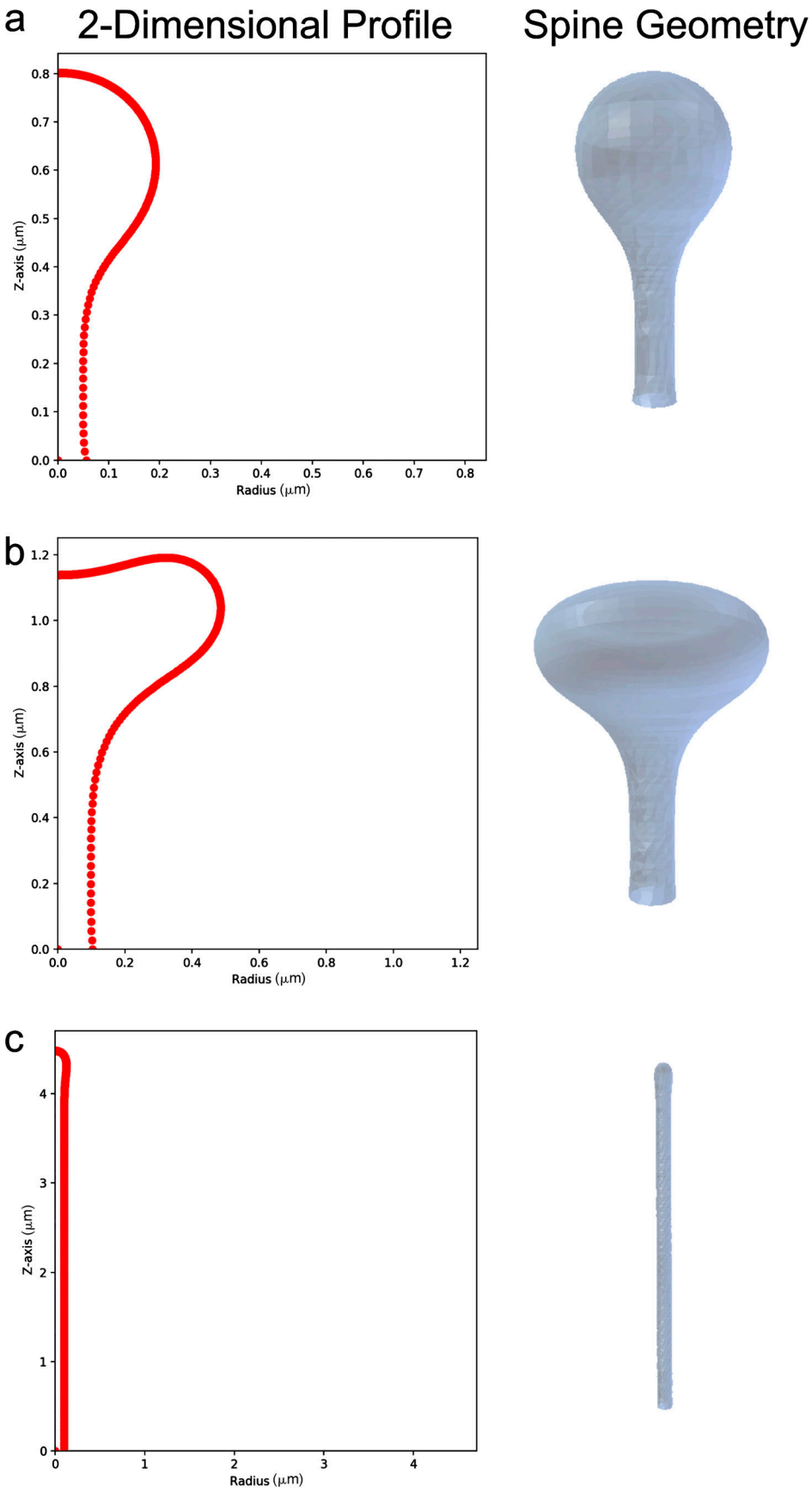

Figure S1. **2-D spine profiles. (a–c)** The 2-D spine profiles and the resultant rotationally symmetric spine geometries for thin spines (a), mushroom spines (b), and filopodia (c).

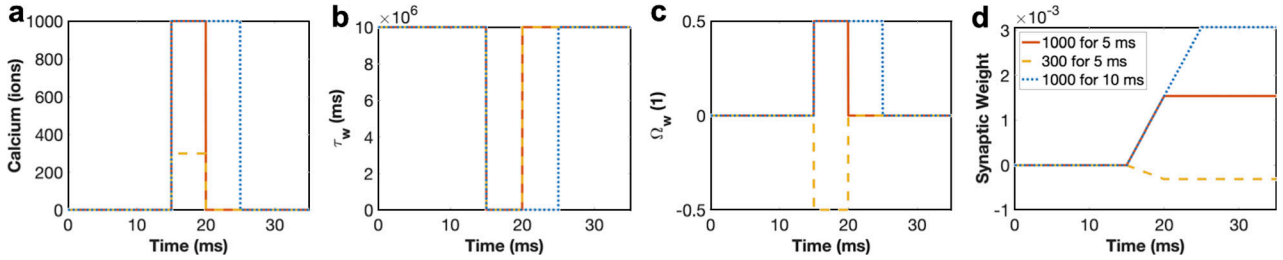

Figure S2. **Artificial calcium transients demonstrate how learning rate, Ωw, and synaptic weight depend on calcium temporal dynamics. (a–d)** To illustrate the relationship between calcium (a), τw (b), Ωw (c), and synaptic weight (d), we constructed three artificial calcium profiles with Heaviside functions. The calcium profiles are (1) 1,000 ions for 5 ms (red line), (2) 300 ions for 5 ms (yellow dashed line), and (3) 1,000 ions for 10 ms (blue dotted line).

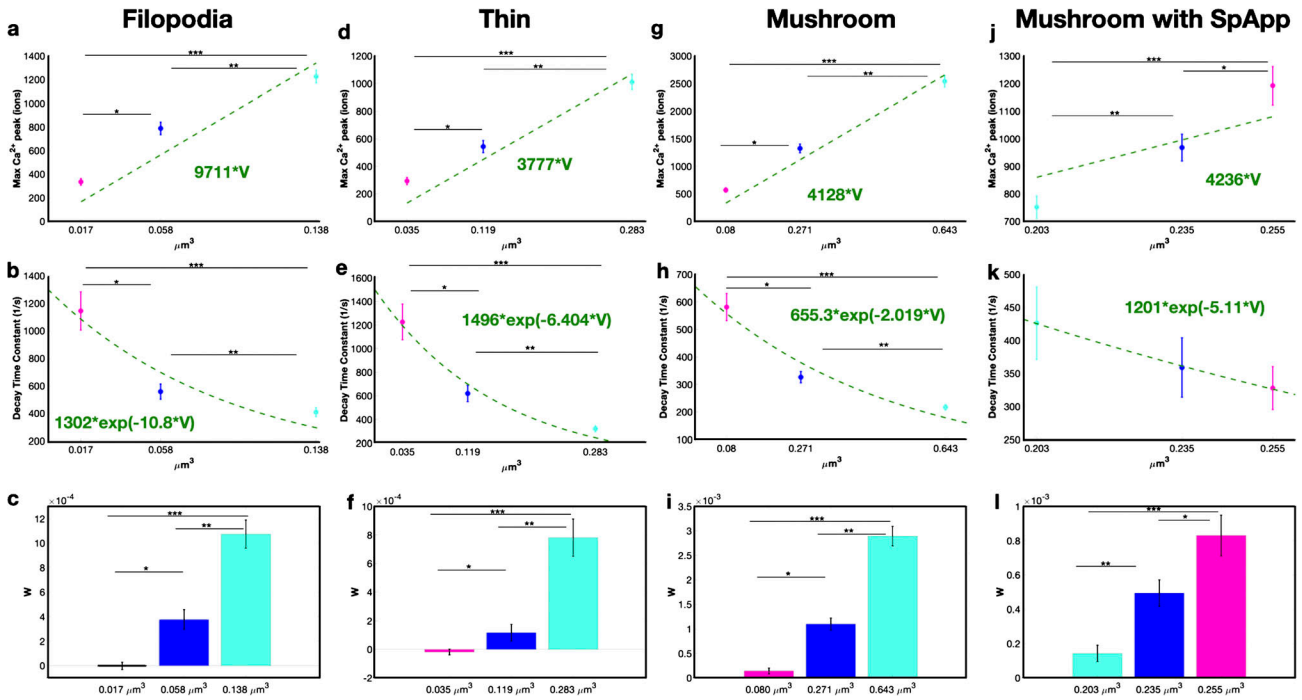

Figure S3. **Trends across volume are similar to trends across volume-to-surface-area ratio.** Peak calcium levels, decay time constant, and synaptic weight updates for size variations given as volumes for filopodia-shaped spines (a–c), thin spines (d–f), mushroom spines (g–i), and mushroom spines with SpApp (j–l). Peak calcium is fitted with a line with a fixed zero intercept. *, **, and *** denote statistically significant values between the different sized spines. P values for each comparison are shown in Fig. S12.

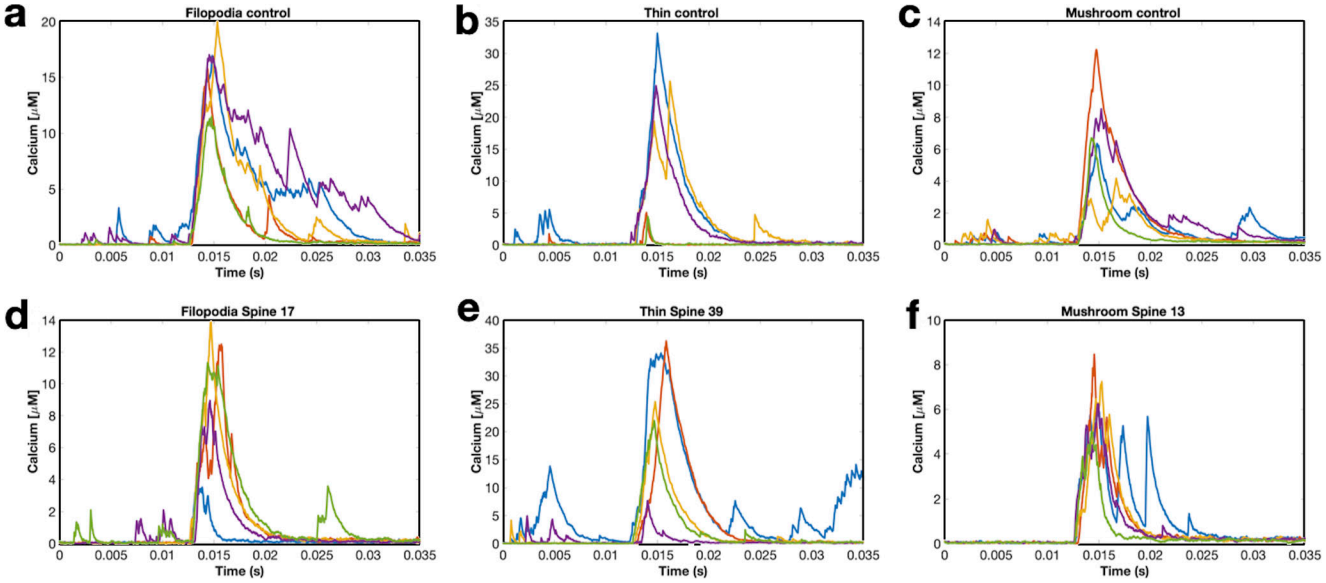

Figure S4. **Examples of calcium transients in terms of concentration for various geometries.** Five examples of calcium transients in terms of concentration for the filopodia control geometry (a), thin control geometry (b), mushroom control geometry (c), realistic filopodia spine 17 (d), realistic thin spine 39 (e), and realistic mushroom spine 13 (f).

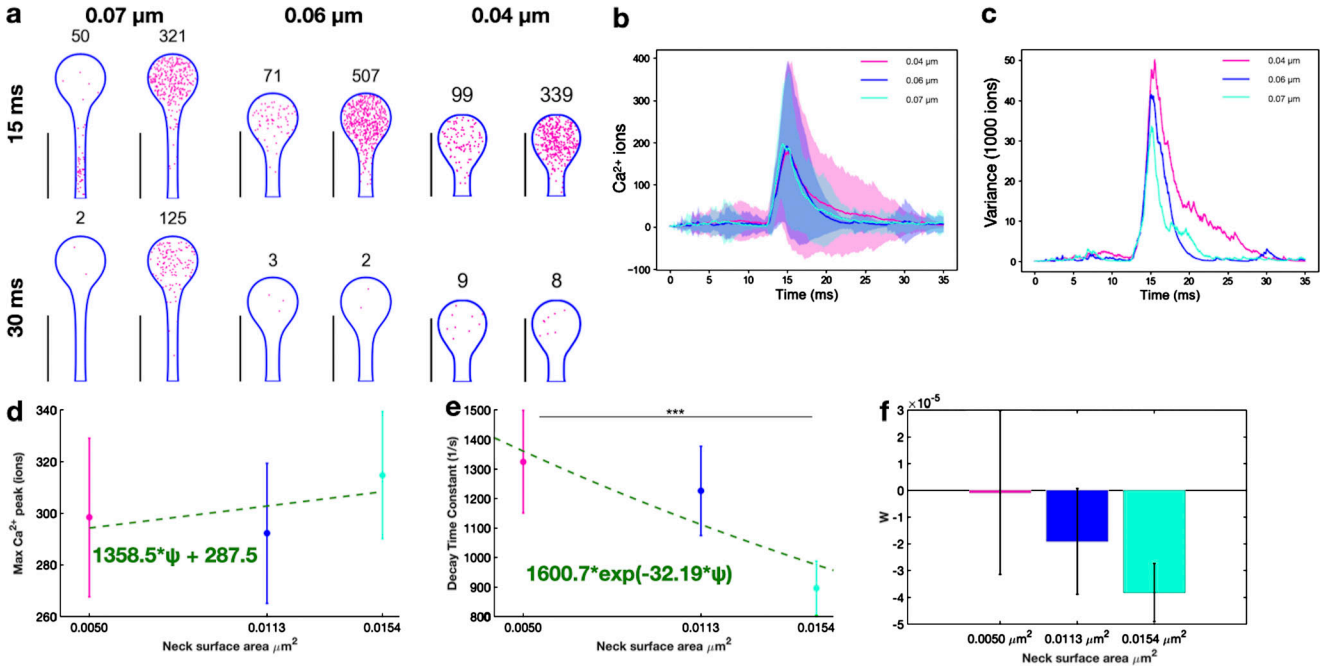

Figure S5. **Effect of spine neck variation on synaptic plasticity in thin spines. (a)** Spatial plots at 15 and 30 ms for thin spines of the same volume with different neck geometries (neck radius of 0.04, 0.06, and 0.07 μm). The number above each spine corresponds to the number of calcium ions present at that time point. Scale bar, 2 μm. **(b and c)** Calcium ions over time (b) and variance, displayed as variance divided by 1,000 ions (c), for all three thin spines with different neck cases. Shaded regions in b denote SD. **(d)** Peak calcium ion number for each thin spine with the mean and SEM (n = 50) show no statistically significant differences using a two-tailed t test. We fitted the trend in peak calcium as a linear function of spine neck base surface area; r^2 = 0.0009 for the linear fit. **(e)** We fitted the decay portion of each calcium transient with the exponential decay function $c \cdot \exp(-kt)$. The decay time constant mean and SEM (n = 50), k, only statistically significant differences shows between the thin and thick necks; ***, P = 0.0322 from two-tailed t test. We fitted the trend in decay time constants as a function of spine neck base surface area with an exponential $a \cdot \exp(-b\psi)$, where ψ is the spine neck base surface area; r^2 = 0.0256 for the exponential fit. **(f)** Calculated synaptic weight change at the last time point for all three thin spines shows no statistically significant difference due to neck size.

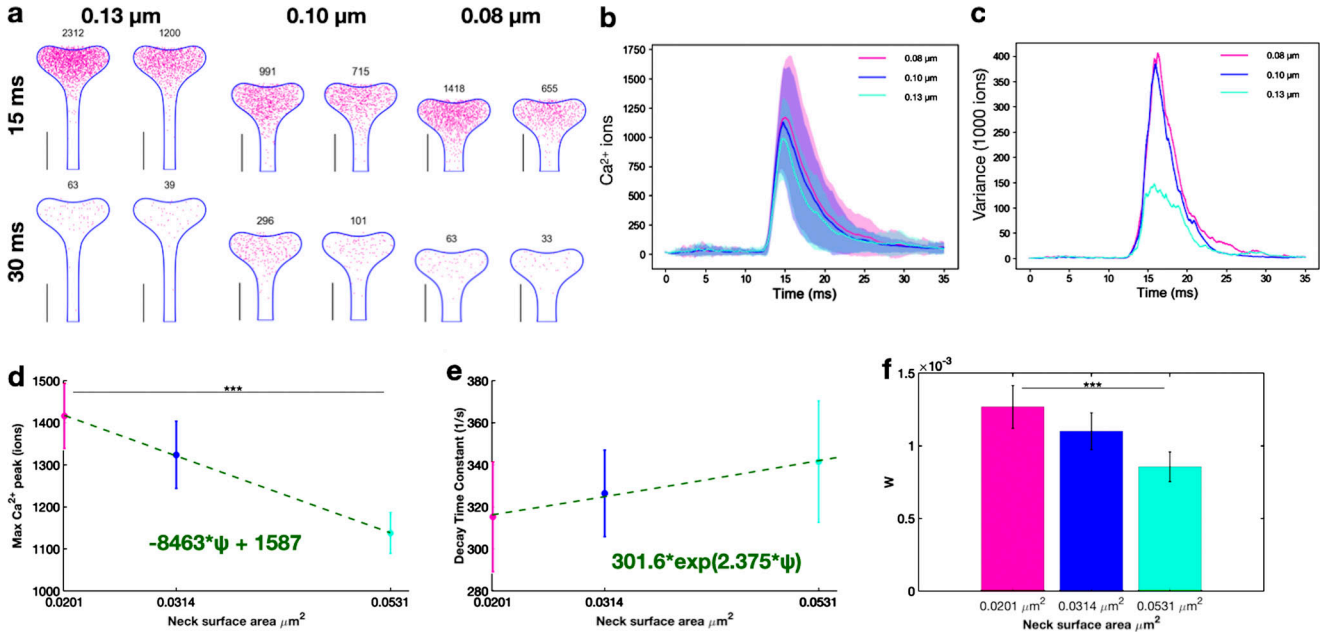

Figure S6. **Effect of spine neck variation on synaptic plasticity in mushroom spines. (a)** Spatial plots at 15 and 30 ms for mushroom spines of the same volume with different neck geometries (neck radius of 0.08, 0.10, and 0.13 µm). The number above each spine corresponds to the number of calcium ions present at that time point. Scale bar, 2 µm. **(b and c)** Calcium ions over time (b) and variance, displayed as variance divided by 1,000 ions (c), for all three mushroom spines with different neck cases. Shaded regions in b denote SD. **(d)** Peak calcium ion number for each mushroom spine with the mean and SEM (n = 50) show statistically significant differences between the thin and thick spines; ***, P = 0.0029 using a two-tailed t test. We fitted the trend in peak calcium as a linear function of spine neck base surface area; r^2 = 0.0528 for the linear fit. **(e)** We fitted the decay portion of each calcium transient with the exponential decay function $c \cdot \exp(-kt)$. The decay time constant mean and SEM (n = 50), k, shows no statistically significant differences from a two-tailed t test. We fitted the trend in decay time constants as a function of spine neck base surface area with an exponential $a \cdot \exp(-b\psi)$, where ψ is the spine neck base surface area; r^2 = 0.0036 for the exponential fit. **(f)** Calculated synaptic weight change at the last time point for all three mushroom spines shows a statistically significant difference only between the thin and thick spines, ***, P = 0.0244 from two-tailed t test.

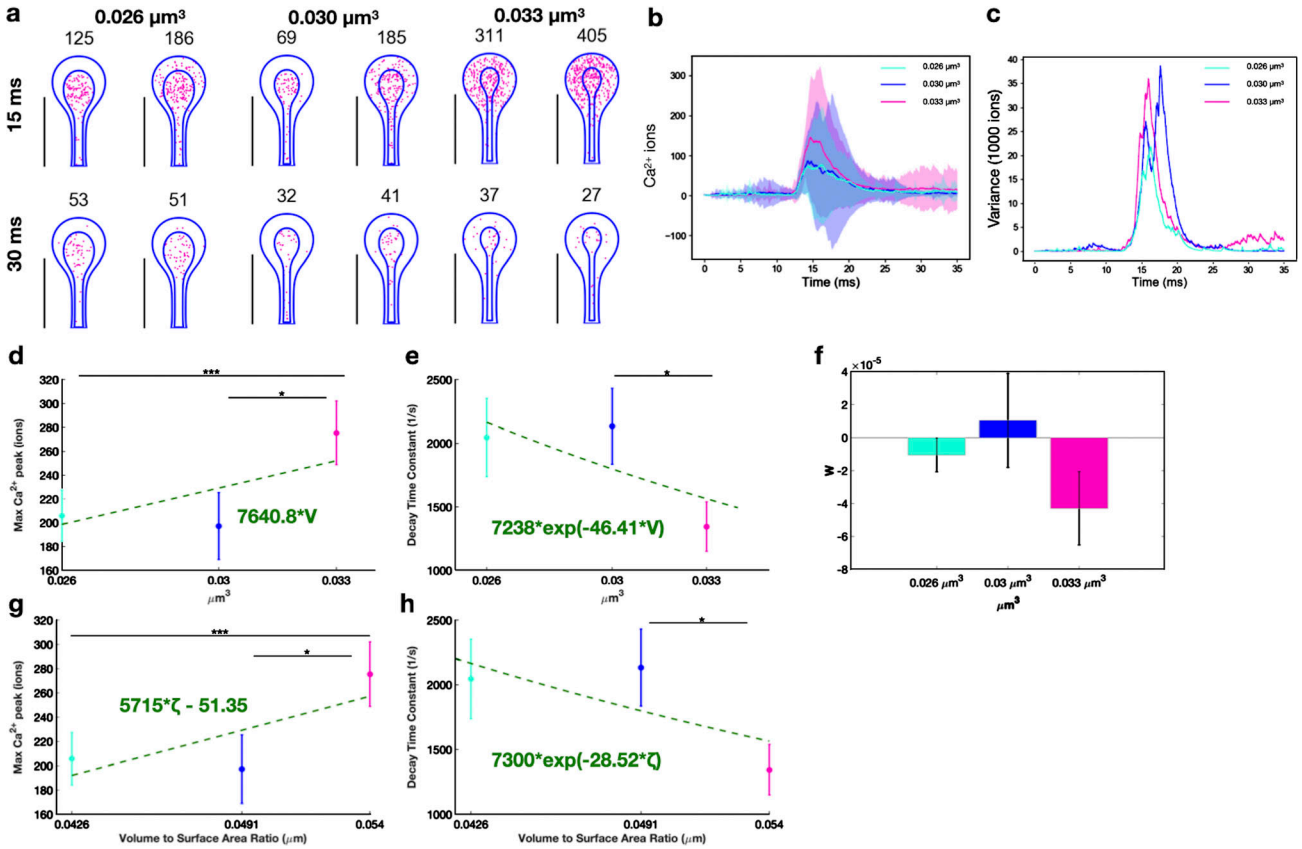

Figure S7. **Sp App size modulates synaptic weight change in thin spines. (a)** Spatial plots at 15 and 30 ms for thin spines with SpApp of different volumes (spine cytosolic volumes of 0.026, 0.030, and 0.033 μm^3). The numbers on top of the shape indicate the total number of calcium ions at that instant in both the SpApp and cytoplasm. **(b and c)** Calcium ions over time as mean and SD (b) and variance, displayed as variance divided by 1,000 ions (c), for all three thin spines with different SpApp sizes. Shaded regions in b denote SD. **(d)** Peak calcium ion number for each thin spine with a SpApp, with the mean and SEM (n = 50), show statistically significant differences between two of the three paired cases; *, P = 0.0461; ***, P = 0.0453 from two-tailed t test. We fitted the trend in peak values with a linear function against the cytoplasm volume; r^2 = 0.0145 for the linear fit. **(e)** We fitted the decay dynamics of each calcium transient with $c \cdot \exp(-kt)$ and report the decay time constant, k, as a mean and SEM (n = 50). We found statistically significant differences only between the second and third spines; *, P = 0.0289 from a two-tailed t test. We fitted the trend in decay time constants as a function of cytosolic volume with an exponential $a \cdot \exp(-bV)$, where V is the cytosolic volume; r^2 = 0.0177 for the fit. **(f)** Calculated synaptic weight change at the last time point for all three thin spines shows no statistically significant difference due to SpApp size. **(g and h)** We also plotted peak calcium ion number and decay time constant against the cytosolic volume-to-surface-area ratio (g and h, respectively). **(g)** We fitted the trend in peak values with a linear function against the volume-to-surface-area ratio; r^2 = 0.0214 for the linear fit. **(h)** We fitted the trend in decay time constants as a function of volume-to-surface-area ratio with an exponential $a \cdot \exp(-b\zeta)$, where ζ is the volume-to-surface-area ratio; r^2 = 0.0178 for the fit.

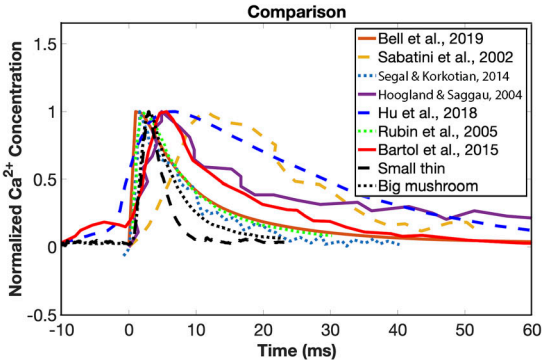

Figure S8. **Normalized calcium transients from different experimental and computational studies.** We plotted the temporal dynamics of the small idealized thin spine (0.035 µm³) and large idealized mushroom spine (0.643 µm³) versus reported experimental calcium transients from previous studies (Sabatini et al.,2002; Hoogland and Saggau, 2004; Segal and Korkotian, 2014) and computational model results from previous studies (Bell et al., 2019; Bartol et al., 2015; Rubin et al., 2005; Hu et al., 2018). The various experimental transients are reported in terms of fluorescence, and we assumed the transients were linearly proportional to concentration (Yasuda et al., 2004). We normalized the various transients and time shifted them for a more direct comparison. We plotted from Fig. 1 f in Sabatini et al. (2002), Fig. 1 in Segal and Korkotian (2014), and Fig. 2 d in Hoogland and Saggau (2004). We also compared Fig. 3 of Bell et al. (2019), Fig. 5 of Hu et al. (2018), Fig. 1 a of Rubin et al. (2005), and Fig. 7 i of Bartol et al. (2015).

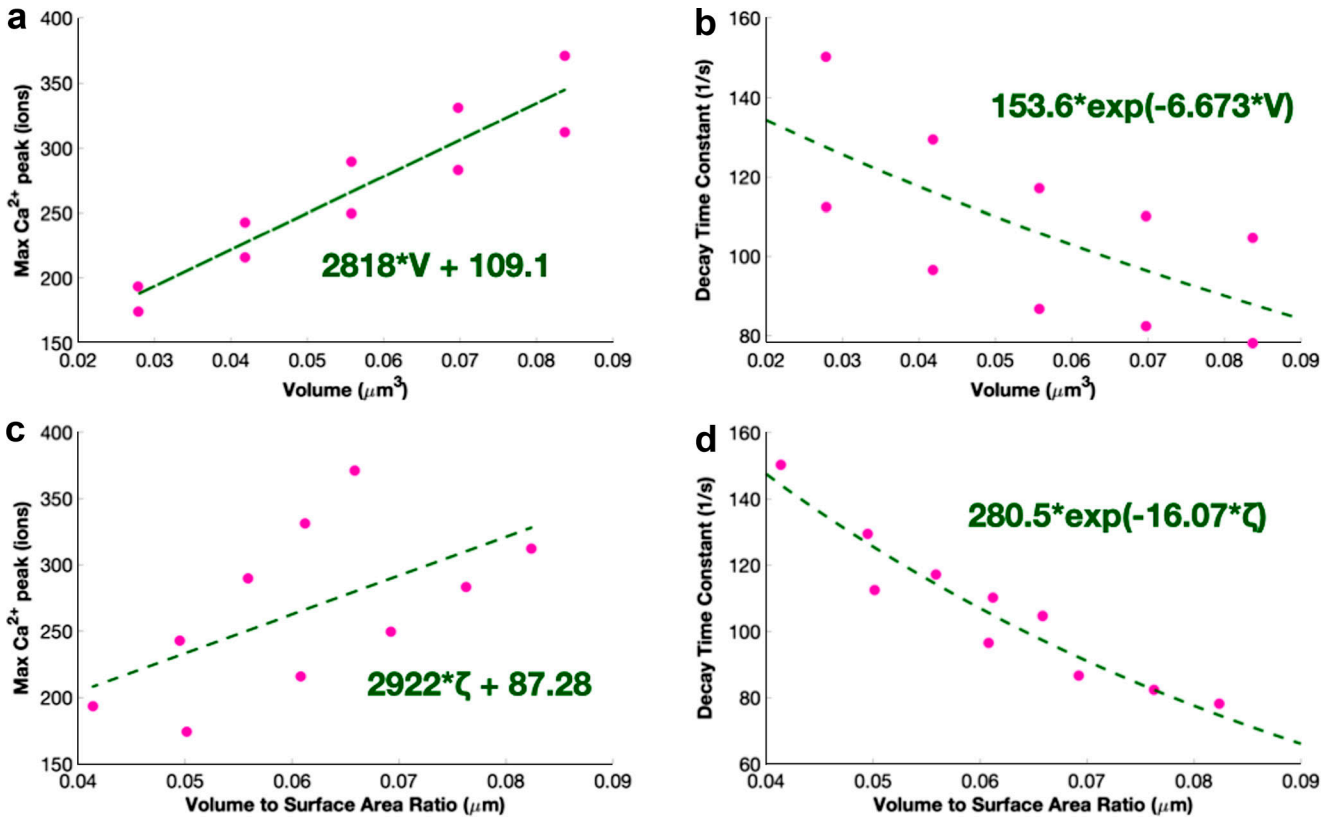

Figure S9. **Previous calcium simulation results match the qualitative trends in these results. (a)** We fitted the trend in peak values with a linear function against the cytoplasm volume; r^2 = 0.8776 for the linear fit. We fixed the y intercept at zero. **(b)** We fitted the decay dynamics of each calcium transient with $c \cdot \exp(-kt)$ and report the decay time constant, k. We fitted the trend in decay time constants as a function of cytosolic volume with an exponential $a \cdot \exp(-bV)$, where V is the cytosolic volume; r^2 = 0.4283 for the fit. **(c)** We fitted the trend in peak values with a linear function against the volume-to-surface-area ratio; r^2 = 0.3492 for the linear fit. **(d)** We fitted the trend in decay time constants as a function of volume-to-surface-area ratio with an exponential $a \cdot \exp(-b\zeta)$, where ζ is the volume-to-surface-area ratio; r^2 = 0.9054 for the fit.

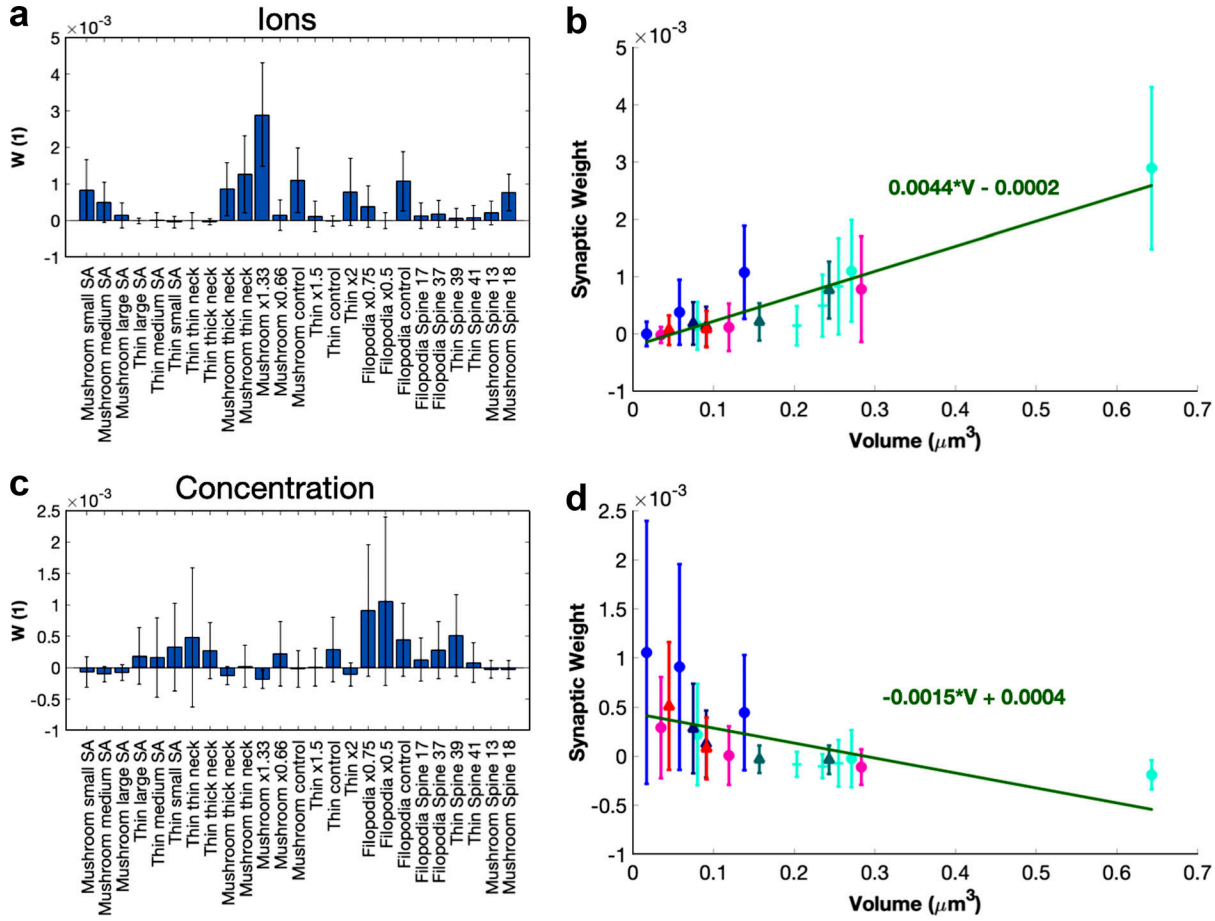

Figure S10. **Synaptic weight updates when considering Ca^{2+} in terms of ions or concentration. (a–d)** Synaptic weight updates for each stochastic idealized and real geometry simulation when synaptic weight calculations are in terms of ions (a and b) and concentration (c and d). We plotted the synaptic weight changes against the spine volume for calculations using ions (b) and concentration (d). We fitted the trends using a linear function of volume; r^2 = 0.4635 for the ion fit and r^2 = 0.1229 for the concentration fit.

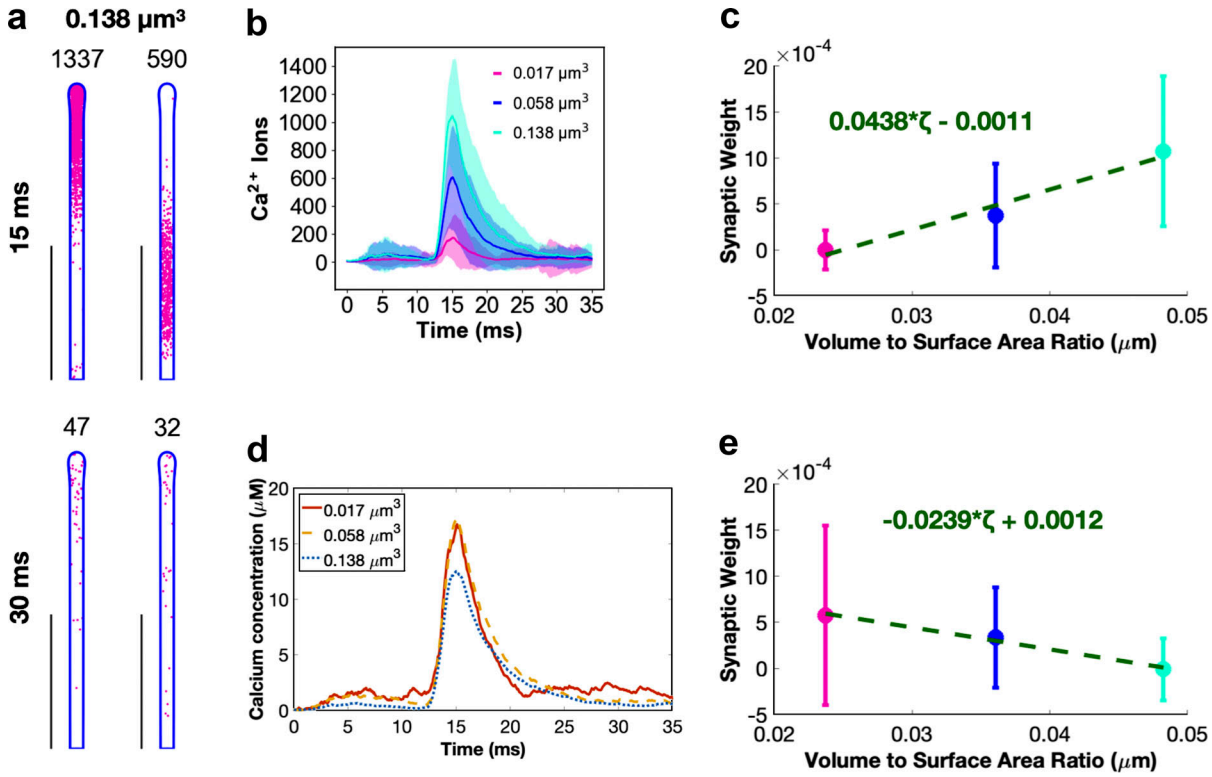

Figure S11. **Synaptic weight updates when considering Ca^{2+} in terms of ions or concentration for the filopodia-shaped spines. (a)** Spatial plots illustrating Ca^{2+} localization at 15 and 30 ms for a filopodia-shaped spine with volume 0.138 µm³. The number above each geometry corresponds to the number of Ca^{2+} in that frame. Two random seeds are shown. Scale bars, 2 µm. **(b)** Mean (solid) and SD (shaded area) of Ca^{2+} transients across 50 simulations for each of the three filopodia-shaped spine sizes (0.017, 0.058, and 0.138 µm³). **(c)** Synaptic weight prediction for each of the filopodia geometries calculated as a function of total calcium ions. We fitted the trends using a linear function of volume-to-surface-area ratio; $r^2 = 0.3594$ for the ion fit. **(d)** Mean of the calcium transients for each filopodia-shaped spine size converted to concentration. **(e)** Synaptic weight prediction for each of the filopodia geometries calculated as a function of calcium concentration. We fitted the trends using a linear function of volume-to-surface-area ratio; $r^2 = 0.1143$ for the concentration fit. We found statistically significant differences between the first and third spines and between the second and third spines; $P_{12} = 0.1301$; $P_{23} = 2.2567 \times 10^{-4}$; $P_{13} = 1.1347 \times 10^{-4}$ from two-tailed *t* test, where 1, 2, and 3 correspond to the spines in increasing volume.

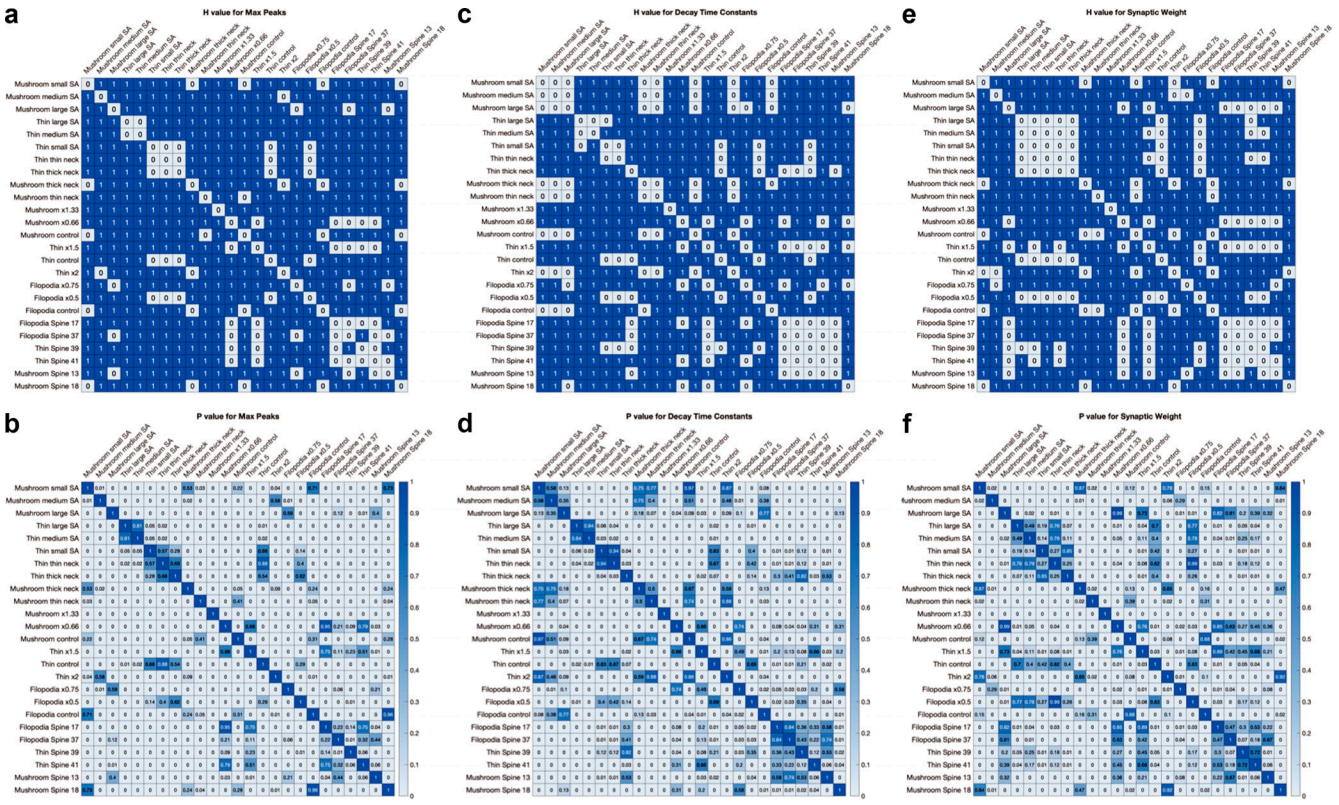

Figure S12. **Two-tailed *t* test comparison between all simulations.** We conducted two-tailed *t* tests between all simulations and display the *h* value and P value for maximum Ca^{2+} peaks (a and b), decay rate constant (c and d), and synaptic weight change (e and f). Displayed P values are truncated at two decimal points.

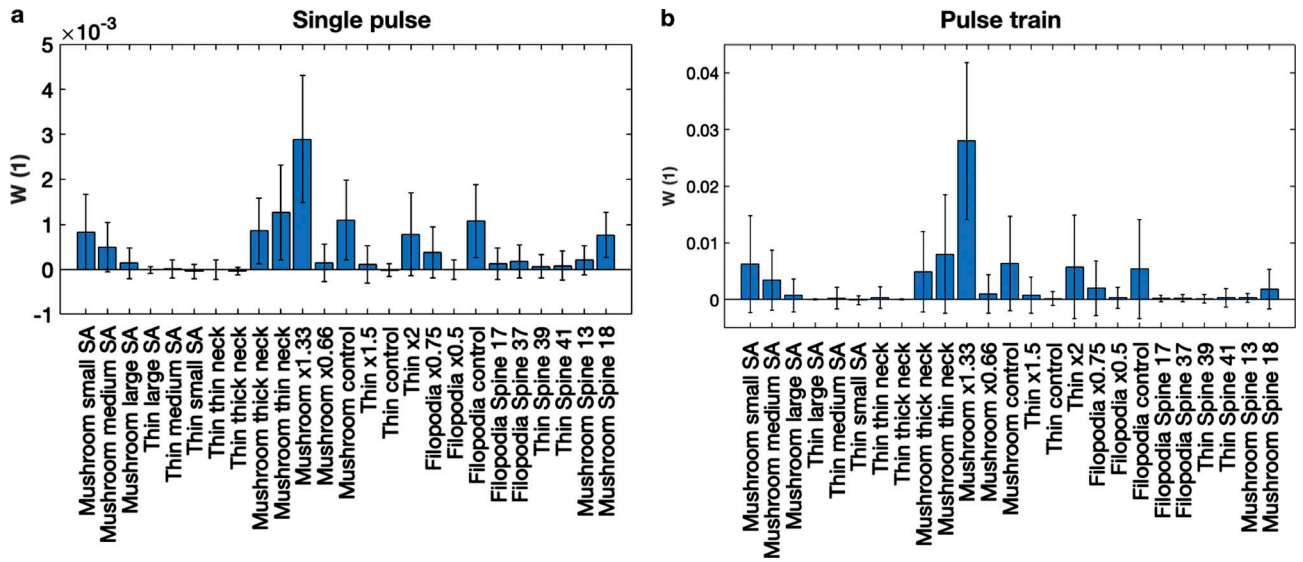

Figure S13. **Single pulses and multiple pulses show similar trends in synaptic weight updates across different geometries. (a)** Synaptic weight change due to a single pulse of calcium for the different spine geometries. **(b)** Synaptic weight change due to multiple pulses of calcium for the different spine geometries.

Video 1. **Sample video of idealized filopodia simulation.** A single seed of an idealized filopodia simulation is shown for the whole time period from 0 to 35 ms. The PM mesh is shown in blue and the Ca^{2+} ions are red.

Video 2. **Sample video of idealized thin spine simulation.** A single seed of an idealized thin spine simulation is shown for the whole time period from 0 to 35 ms. The PM mesh is shown in blue and the Ca^{2+} ions are red.

Video 3. **Sample video of idealized mushroom spine simulation.** A single seed of an idealized mushroom spine simulation is shown for the whole time period from 0 to 35 ms. The PM mesh is shown in blue and the Ca^{2+} ions are red.

Video 4. **Sample video of idealized mushroom spine with a SpApp simulation.** A single seed of an idealized mushroom spine with a SpApp simulation is shown for the whole time period from 0 to 35 ms. The PM and SpApp membrane mesh are shown in blue and the Ca^{2+} ions are red.

Video 5. **Sample video of realistic filopodia 17 simulation.** A single seed of a realistic filopodia 17 simulation is shown for the whole time period from 0 to 35 ms. The PM mesh is shown in blue and the Ca^{2+} ions are red.

Video 6. **Sample video of realistic filopodia 37 simulation.** A single seed of a realistic filopodia 37 simulation is shown for the whole time period from 0 to 35 ms. The PM mesh is shown in blue and the Ca^{2+} ions are red.

Video 7. **Sample video of realistic thin spine 39 simulation.** A single seed of a realistic thin spine 39 simulation is shown for the whole time period from 0 to 35 ms. The PM mesh is shown in blue and the Ca^{2+} ions are red.

Video 8. **Sample video of realistic thin spine 41 simulation.** A single seed of a realistic thin spine 41 simulation is shown for the whole time period from 0 to 35 ms. The PM mesh is shown in blue and the Ca^{2+} ions are red.

Video 9. **Sample video of realistic mushroom spine 13 simulation.** A single seed of a realistic mushroom spine 13 simulation is shown for the whole time period from 0 to 35 ms. The PM mesh is shown in blue and the Ca^{2+} ions are red.

Video 10. **Sample video of realistic mushroom spine 18 simulation.** A single seed of a realistic mushroom spine 18 simulation is shown for the whole time period from 0 to 35 ms. The PM mesh is shown in blue and the Ca^{2+} ions are red.

Provided online are Table S1, Table S2, and Table S3. Table S1 and Table S2 list all geometric variations. Table S3 lists values for realistic geometries.